



저작자표시-비영리-동일조건변경허락 2.0 대한민국

이용자는 아래의 조건을 따르는 경우에 한하여 자유롭게

- 이 저작물을 복제, 배포, 전송, 전시, 공연 및 방송할 수 있습니다.
- 이차적 저작물을 작성할 수 있습니다.

다음과 같은 조건을 따라야 합니다:



저작자표시. 귀하는 원저작자를 표시하여야 합니다.



비영리. 귀하는 이 저작물을 영리 목적으로 이용할 수 없습니다.



동일조건변경허락. 귀하가 이 저작물을 개작, 변형 또는 가공했을 경우에는, 이 저작물과 동일한 이용허락조건하에서만 배포할 수 있습니다.

- 귀하는, 이 저작물의 재이용이나 배포의 경우, 이 저작물에 적용된 이용허락조건을 명확하게 나타내어야 합니다.
- 저작권자로부터 별도의 허가를 받으면 이러한 조건들은 적용되지 않습니다.

저작권법에 따른 이용자의 권리는 위의 내용에 의하여 영향을 받지 않습니다.

이것은 [이용허락규약\(Legal Code\)](#)을 이해하기 쉽게 요약한 것입니다.

[Disclaimer](#)

공학석사 학위논문

**Synthesis, Photophysics and
Applications of Organic Excited-
state Intramolecular Proton
Transfer (ESIPT) Materials**

2012년 8월

여기상태 분자내 양성자 이동 물질의 합성, 광물리

과정 분석 및 응용

서울대학교 대학원

재료공학부

이 중 하

**Synthesis, Photophysics and Applications of
Organic Excited-state Intramolecular Proton
Transfer (ESIPT) Materials**

여기상태 분자내 양성자 이동 물질의 합성, 광물리 과정
분석 및 응용에 관한 연구

지도 교수 박 수 영

이 논문을 공학석사 학위논문으로 제출함
2012 년 8 월

서울대학교 대학원

재료공학부

이 종 하

이종하의 공학석사 학위논문을 인준함
2012 년 8 월

위 원 장 _____ (인)

부위원장 _____ (인)

위 원 _____ (인)

**Synthesis, Photophysics and Applications of
Organic Excited-state Intramolecular Proton
Transfer (ESIPT) Materials**

A THESIS SUBMITTED IN PARTIAL FULFILLMENT OF
THE REQUESTMENTS FOR THE DEGREE OF MASTER
IN ENGINEERING AT THE GRADUATE SCHOOL OF
SEOUL NATIONAL UNIVERSITY

August 2012

BY

Jongha Lee

Supervisor

Soo Young Park

Abstract

Synthesis, Photophysics and Applications of Organic Excited-state Intramolecular Proton Transfer (ESIPT) Materials

Jongha Lee

Department of Materials Science and Engineering

The Graduate School

Seoul National University

Fluorescent excited-state intramolecular proton transfer (ESIPT) materials have attracted considerable research interests due to their unique properties; absence of self-absorption, strongly fluorescent properties and environment sensitive emission behaviors. Such ESIPT materials have been utilized for organic light-emitting diodes (OLED), organic dye laser, UV stabilizer and fluorescent chemo-sensor. Here, I report the design, synthesis, photophysics and applications of new ESIPT materials which emanate strong photoluminescence in solid state. Developed materials show enhanced

emission in solid state rather than solution state, which is known for 'aggregation-induced enhanced emission (AIEE)' in contrast concentration quenching effect observed from common fluorophore. These are due to aggregation mediated planarization and J-aggregated formation or combination of steric crowding around the fluorophore and restriction of intramolecular rotation (RIR) which is known for main non-radiative decay process.

Based on these photophysics study, π -conjugated low-molecular weight organogelator (LMOG) containing central salicylideneaniline moiety, ESIPT fluorophore, was designed and synthesized. The molecule easily aggregates into 1-D nano-ribbon architecture with enhanced fluorescence property. In addition, the organogel system is responsive toward biologically important fluoride anion, which has potential application for solidic anion detection kit.

Fluorescent imidazole molecules have applied for organic electroluminescence device and its unique delayed fluorescence property was reported previously. In this study, I investigate the naphthyl substitution effects on thermal, electrochemical and optical property for better dyes toward better OLED application. Naphthyl substituted imidazole possess higher glass transition temperature (T_g) for durable thermal stability and lower LUMO level which is beneficial for efficient electron injection.

Moreover, I propose a new mechanism of ‘spin-harvesting’ device in HPI molecule harnessing thermally activated delayed fluorescence (TADF).

Keywords: Excited-state intramolecular proton transfer (ESIPT), Aggregation-induced enhanced emission (AIEE), delayed fluorescence, smart-gel, electroluminescence, spin-harvesting.

Student Number: 2010-22766

Contents

Abstract	i
Contents	iv
List of Schemes	vi
List of Figures	vii
List of Tables	xiv
Chapter 1 Introduction	1
1.1 Radiative Decay Process of Excited Organic Molecule.....	1
1.2 Excited-State Intramolecular Proton Transfer	8
1.3 Luminescent behavior in solid state.....	10
1.4 Research Objectives.....	14
1.5 References	15
Chapter 2 Simple π-conjugated Low Molecular-Weight Organogelator (LMOG) Showing Excited-state Intramolecular Proton Transfer for Anion detection.	18
2.1 Introduction	18

2.2	Result and Discussion	20
2.3	Conclusion.....	41
2.4	Experimental.....	42
2.5	References	49

Chapter 3 Excited-state Intramolecular Proton Transfer (ESIPT) Mediated Spin Up-conversion of Triplet Excitons toward Highly Efficient Blue OLED Devices: effect of naphthyl substitution53

3.1	Introduction	53
3.2	Result and Discussion	55
3.3	Conclusion.....	83
3.4	Experimental.....	84
3.5	References	87

Abstract in Korean.....89

List of Presentations.....92

List of Schemes

Scheme 1.1 Molecular structure of representative ESIPT-exhibiting fluorescent dyes.....	9
Scheme 1.2 Molecular structure of several aggregation-induced emission enhancement (AIEE) active dyes.....	13
Scheme 2.1 Chemical structure of organogelator, 1 and control compound, 2	13
Scheme 2.2 Overall synthetic routes to 1 and 2	44
Scheme 3.1 Molecular Structure of HPI derivatives designed and synthesized..	58
Scheme 3.2 four-level photocycle and delayed fluorescence of HPI series molecule.	71
Scheme 3.3 Proposed spin-harvesting process of HPI molecules.....	82

List of Figures

Figure 1.1 Jablonski diagram of transition between different electronic or vibrational energy level.	3
Figure 1.2 Spectrum of absorption and emission spectra from Wikipedia.	7
Figure 1.3 Schematic four-level energy diagram of ESIPT cycle.....	10
Figure 2.1 (a) Optical and (b) fluorescence ($\lambda_{\text{ex}} = 365$ nm) microscope images of xerogel of 1 casted on a glass substrate. FE-SEM images of xerogel of 1 under 15.0 kV. The scale bar indicates (c) 50 μm and (d) 5 μm	22
Figure 2.2 Comparison of normalized UV-Vis absorption (solid) and fluorescence (solid-dot) spectra of 1 solution (black; 10 μM , 1,2-dichloroethane) and xerogel (blue; 0.1 wt % in sodium chloride solid solution. Diffuse reflectance technique was employed for the measurement of the UV-vis absorption spectrum.	24
Figure 2.3 Fluorescence spectrum of 1 with concentration of 2.0 wt% in 1,2-dichloroethane hot solution (blue) and	

after gelation	25
Figure 2.4 (a) XRD profile of xerogel 1 . (b) Optimized molecular length of 1 from quantum chemical calculations with Gaussian 09 software package (c) Suggested packing structure of 1 in gel state.	26
Figure 2.5 (a) Small angle X-ray scattering (SAXS) and (b) Wide angle X-ray scattering (WAXS) profiles of xerogel 1 casted on glass substrate.....	28
Figure 2.6 Electrostatic potential isosurfaces of 1 and 2 . Gaussian 09 software package was employed for the quantum chemical calculations. Potential ranges were set to constant value from -1.600E-2 to +1.600E-2	29
Figure 2.7 Image of drop-casted film (2.0 wt% in 1,2-dichloroethane) of 2	30
Figure 2.8 Fluoride ion induces collapse of organogel formed in 1,2-dichloroethane (2.0 wt %, 1.00 g): (a) fluorescence emission of as-prepared organogel under photoexcitation at 365 nm; (b) absorption colour of as-prepared organogel; (c) (f) time course of the collapse of organogel by TBAF, (c) 0 min, (d) 10 min, (e) 20 min, (f) 30	

min; (g) fully collapsed organogel, (h) collapsed organogel under photoexcitation at 365 nm; (i) after addition of 0.1 mL of methanol and then heated and cooled to re-form organogel.32

Figure 2.9 Fluorescence spectrum of (black) organogel of **1** (1,2-dichloroethane) and (red) 30 minutes after addition of TBAF.33

Figure 2.10 Acetate ion induces collapse of organogel formed in 1,2-dichloroethane (2.0 wt %, 1.00 g): time course of the collapse of organogel by TBAF, (a) 0 min, (b) 10 min, (c) 20 min, (d) 30 min and (e) 40 min34

Figure 2.11 (a) UV-vis absorption and (b) fluorescence ($\lambda_{\text{ex}} = 405 \text{ nm}$) spectral change of **1** (40 μM in THF) with the addition of tetrabutylammonium fluoride (TBAF) solution from 0 equiv. to 5 equiv. by 0.2 equiv. (c) Schematic representation of a mechanism for fluorescence change of **1** in response to fluoride ion. (d) Electrostatic potential isosurfaces of deprotonated **1** and **1**. Gaussian 09 software package was employed for the quantum chemical calculations36

Figure 2.12 (a) Job's plot from the absorbance at 481 nm. The total ion concentration $[F^-]+[1] = 100 \mu\text{M}$ (b) Benesi-Hildebrand plot by utilizing absorbance at 365 nm.....	37
Figure 2.13 ^1H NMR titration of 1.0 mM of 1 and specific concentration of TBAF.	38
Figure 2.14 ^{19}F NMR spectra from mixture of 1.0 mM of 1 and 1.0 mM of TBAF. -63.50 ppm and -63.57 ppm indicates two trifluoromethyl groups, -117.96 ppm indicates tetrabutylammonium fluoride salts and -153.09 ppm indicates HF_2^- anion	39
Figure 3.1 Molecular structure and the numbering of phenyl rings of basic HPI molecule.....	57
Figure 3.2 Normalized absorbance and PL of HPI, HPI-Cbz, HPIN, HPIN-Cbz compounds... ..	60
Figure 3.3 Normalized absorbance and normalized HPI, HPIN, their difference and comparison with MeOPIN.	61
Figure 3.4 Optimized geometry of each tautomer of four compounds. E and K corresponds E and K, respectively... ..	63
Figure 3.5 Differential scanning calorimetric curve of HPIN-Cbz with scan rate of $10 \text{ }^\circ\text{C}/\text{min}$. Inset: magnified	

graph around glass transition temperature (T_g)..	67
Figure 3.6 Thermo gravimetric analyzer (TGA) curve of HPIN-Cbz with scan rate of 10 °C/min.....	68
Figure 3.7 time-resolved emission spectrum of (a) HPI (b) HPIN (c) HPI-Cbz (d) HPIN-Cbz collected at prompt (green), after 10 μ s (black), 1 ms (red) 1 s (blue) after photo-excitation.....	70
Figure 3.8 Energy level location with optimized geometry of figure 3.4.....	73
Figure 3.9 (a) Absorbance change of HPI from 298 K (red) to 77 K (red) (b) Photoluminescence change of HPI from 298 K (red) to 77 K (blue) and phosphorescence (green) (c) time-resolved emission spectrum (phosphorescence) of HPI collected 100 μ s after photo-excitation at 77 K (d) time-resolved emission spectrum of HPI collected 100 μ s after photo-excitation at 117 K. Left peak originate from delayed K^* fluorescence while right one is from K^* phosphorescence.	74
Figure 3.10 (a) Absorbance change of HPI-Cbz from 298 K (red) to 77 K (red) (b) Photoluminescence change of HPI-	

Cbz from 298 K (red) to 77 K (blue) and phosphorescence (green) (c) time-resolved emission spectrum (phosphorescence) of HPI-Cbz collected 100 μ s after photo-excitation at 77 K (d) time-resolved emission spectrum of HPI-Cbz collected 100 μ s after photo-excitation at 117 K. Left peak originate from delayed fluorescence while right one is from phosphorescence.....75

Figure 3.11 (a) Absorbance change of HPIN from 298 K (red) to 77 K (red) (b) Photoluminescence change of HPIN from 298 K (red) to 77 K (blue) and phosphorescence (green) (c) time-resolved emission spectrum (phosphorescence) of HPIN collected 100 μ s after photo-excitation at 77 K (d) time-resolved emission spectrum of HPIN collected 100 μ s after photo-excitation at 117 K. Left peak originate from delayed fluorescence while right one is from phosphorescence.....76

Figure 3.12 (a) Absorbance change of HPIN-Cbz from 298 K (red) to 77 K (red) (b) Photoluminescence change of HPIN-Cbz from 298 K (red) to 77 K (blue) and phosphorescence (green) (c) time-resolved emission

spectrum (phosphorescence) of HPIN-Cbz collected 100 μ s after photo-excitation at 77 K (d) time-resolved emission spectrum of HPIN-Cbz collected 100 μ s after photo-excitation at 117 K. Left peak originate from delayed fluorescence while right one is from phosphorescence.77

Figure 3.13 Cyclic voltammogram (10⁻³M solution in dichloromethane, electrolyte: tetrabutylammonium tetraborate, scan rate: 50mV/sec reference electrode: Ag/Ag⁺): (a) HPIN, (b) HPIN-Cbz...80

List of Tables

Table 3.1 Optical property of HPI derivatives in toluene solution	60
Table 3.2 Photophysical properties of four naphthyl and carbazole tuned HPI derivatives in solution (10 ⁻⁵ M in toluene) state and film (100 nm vacuum deposited on quartz substrate)	64
Table 3.3 Summerized molecular energy level of four HPI derivatives.	79
Table 3.4 Estimated molecular orbital energy level of HPI derivatives. HOMO is estimated from cyclic voltammetry and LUMO comes from the summation of HOMO and optical band gap	79

Chapter 1. Introduction

Recently, molecular photonics has attracted notable research attention due to their harnessing capability of light-material interaction. It concerns with the structure-property relationship and physical processes which result from the interaction of organic molecules with light, ranging from the ultraviolet (UV, 200 nm – 350 nm wavelength), visible (Vis, 400 nm – 700 nm wavelength), even infrared (IR, 700 nm – 2000 nm wavelength). Based on these knowledge, various studies have been investigated for real world applications such as organic light-emitting devices (OLED), organic photovoltaics devices (OPV), bio-imaging, optical sensor, dye laser, etc. In this work, synthesis, design and photophysical properties of newly developed fluorescent organic molecules in solid state have been studied. Furthermore, their applicability toward solidic detection with optical properties change and OLED emitting dye is presented. The following introduction will provide a brief knowledge for molecular photonics in this study.

1.1 Radiative Decay Process of Excited Organic Molecule

1.1.1 Fluorescence and Phosphorescence

Appropriate energy injection such as electromagnetic radiation, chemical reaction and electrical energy could excite electronic, vibrational ground-state (S_0) of organic molecules (see Figure 1.1 absorption). In case of the mode of excitation is absorption of a photon, emission of photons accompanying decay is so-called photoluminescence (PL). When a photon is absorbed by the molecule, the corresponding energy induces the excitation of an electron to form an excited-state molecule S_n ($n = 1, 2, 3\dots$). Subsequent vibrational relaxations and internal conversion (less than 10^{-12} seconds time scale) leads the molecule to the lowest vibrational state of electronic excited-state singlet state (S_1). Fluorescence originates when the S_1 state molecule de-excites to reach vibrational sub-level of S_0 state with the emission of photon with time interval (lifetime, τ) of $10^{-9} \sim 10^{-8}$ seconds (Figure 1.1 fluorescence).¹ Since the vibrational relaxations and internal conversion takes place faster than the fluorescence, only the S_1 state is concerned with the fluorescence spectrum, independent of the excitation wavelength (Kasha's rule).² Compared to fluorescence, phosphorescent materials undergo different emission process. After formation of S_1 state, the spin could reverse (Figure 1.1 intersystem crossing) resulting the molecules to excited-state triplet state (T_1), after coming decay of T_1 with the emission of photon is phosphorescence (see Figure 1.1 phosphorescence).

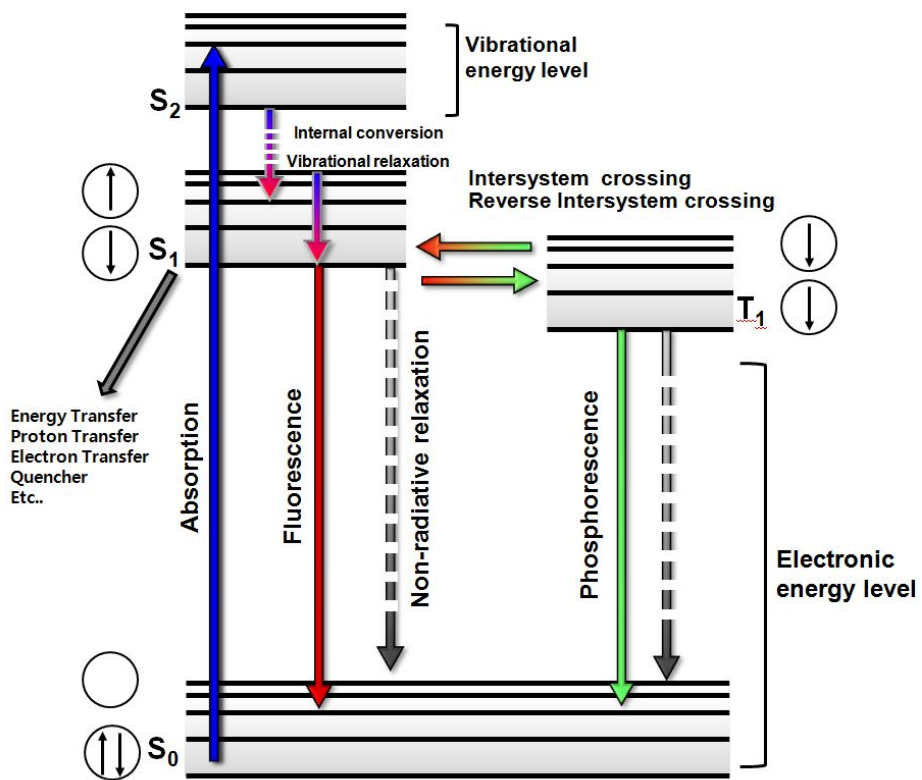


Figure 1.1 Jablonski diagram of transition between different electronic or vibrational energy level.

Also, phosphorescence occurs in longer time scale which is related to spin-forbidden energy transitions in quantum mechanics.³ Ranging from 10^{-6} seconds to several hours of lifetime is often measured. Only few kinds of molecules present the phosphorescence such as heavy metal complexes and aldehyde derivatives of which intersystem crossing could occur within the lifetime of an excited singlet state.

1.1.2 Delayed Fluorescence

When the quencher of triplet state is removed, one may observe enhancement of the intensity and lifetime of fluorescence. Arising components of luminescence referred as “delayed fluorescence” component compared to those of “prompt” fluorescence. This process exhibits the fluorescent characteristic emission spectrum, however, possess different lifetime which is similar to that of phosphorescence. The lifetime of delayed fluorescence is attributed to the participation of triplet state in this process. Indeed, three types of delayed fluorescence are known.⁴

One is E-type delayed fluorescence or thermally activated delayed fluorescence (TADF). T_1 state may thermally popped through the reverse intersystem crossing (Figure 1.1 reverse intersystem crossing) to reach S_1 state, subsequent fluorescent emission from re-formed S_1 state is so-called

TADF. The photophysical sequence of delayed fluorescence is absorption $\rightarrow S_1 \rightarrow T_1 \rightarrow S_1 \rightarrow$ Fluorescence. Since the fluorescence is originated from the population equilibrium of the singlet and triplet state, the lifetimes of delayed fluorescence and the concomitant phosphorescence are similar. Most of TADF is favored in molecules which own small singlet-to-triplet energy gaps such as fullerene,⁵ benzophenone,⁶ Phorphyrin⁷ and imidazole.⁸

Another is referred as P-type delayed fluorescence or triplet-triplet annihilation (TTA). One molecule of S_1 is produced by the interaction of two molecules in the T_1 state. In this bi-photonic process, the lifetime of P-type delayed fluorescence have smaller value of the respective phosphorescence.

The other is recombination fluorescence, the S_1 state becomes populated by recombination of radical ions with electrons or by recombination of radical ions of opposite charge.

1.1.3 Photoluminescence Factors

Photoluminescence (PL) is the phenomenon which the materials absorb photons of a particular wavelength and after time interval, re-emit photons of different wavelength. There are several factors which could characterize the macroscopic photoluminescence properties. As for the PL intensity, absolute PL quantum yield (Φ) plays the most substantial role which could be defined

as the ratio of the number of photons emitted divided by the number of photons absorbed. The absolute quantum yield is independent to the power of the light source and determined only by molecular structure.

Another critical factor is the lifetime, τ . The fluorescence (Phosphorescence) lifetime refers to the average time the molecule stays in its excited state before emitting a photon, typically follows first-order kinetics.

Stokes' shift is the difference between positions of the band maxima of the absorption and emission spectra of the PL (Figure 1.2), specific characteristics of photo-luminescent molecule. According to the Frank-Condon principle, the absorption and emission of light usually occur near spectroscopic minima corresponding to the nuclear geometry of the molecules. Absorption spectra represent the transition from the ground state to different levels of excited states, and the emission spectra represent the transition from the S_1 or T_1 state to corresponding vibrational levels of ground state. Fluorescence and phosphorescence spectrum usually possesses longer wavelength due to the energy loss resulting from the vibrational relaxation and internal conversion, which is Stoke's law.

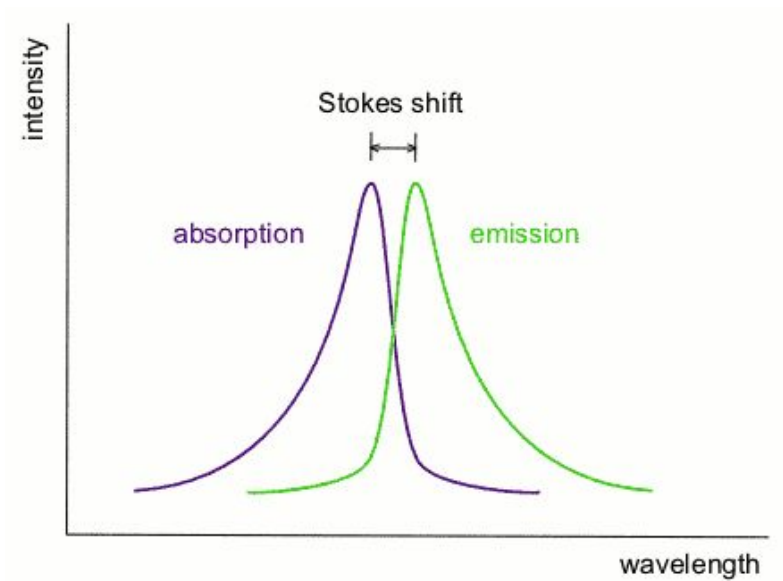
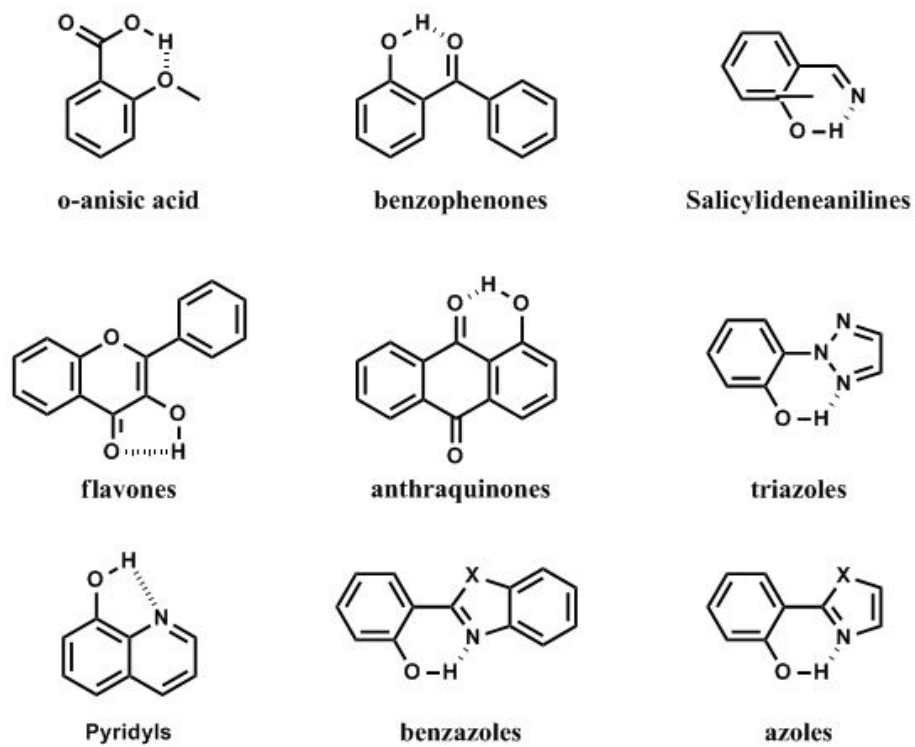


Figure 1.2 Spectrum of absorption and emission spectra from Wikipedia.

1.2 Excited-State Intramolecular Proton Transfer

Excited-state intramolecular proton transfer (ESIPT) is a tautomerization process which occurs in cyclic π -conjugated Brøsted acid (e.g. hydroxyl and amino) and base moieties (amino, sp^2 hybridized nitrogen) under photo-excitation. The typical molecular structure of ESIPT-exhibiting molecule is shown in Scheme 1.1 and Figure 1.3.

In ground state, the molecule exists as a enol (E) form, however, in excited-state, the inversion of acidity and basicity leads the proton transfer, transiently produces a proton-transferred tautomer species, keto form (K^*). Then, the K^* emanates fluorescence or undergoes non-radiative decay. Following back proton transfer restores the original species (E form), completing ESIPT 4-level cycle (Figure 1.3). These ESIPT-exhibiting molecules has attracted great research attention, which is attributed to their unique emission property; large Stokes' shifted fluorescence emission ($6000 - 12000 \text{ cm}^{-1}$), easy population inversion of the K^* and extremely fast process (time scale of 10^{-12} s) and environment sensitive emission behavior. These are because the ESIPT molecules possess different absorbing (E) and emitting (K) properties from the photocycle of E-E*-K*-K*-E process. Owing to these novel optical properties, both theoretical researches of the photophysical process of ESIPT molecule and practical applications have widely investigated. Various ESIPT-



Scheme 1.1 Molecular structure of representative ES IPT-exhibiting fluorescent dyes

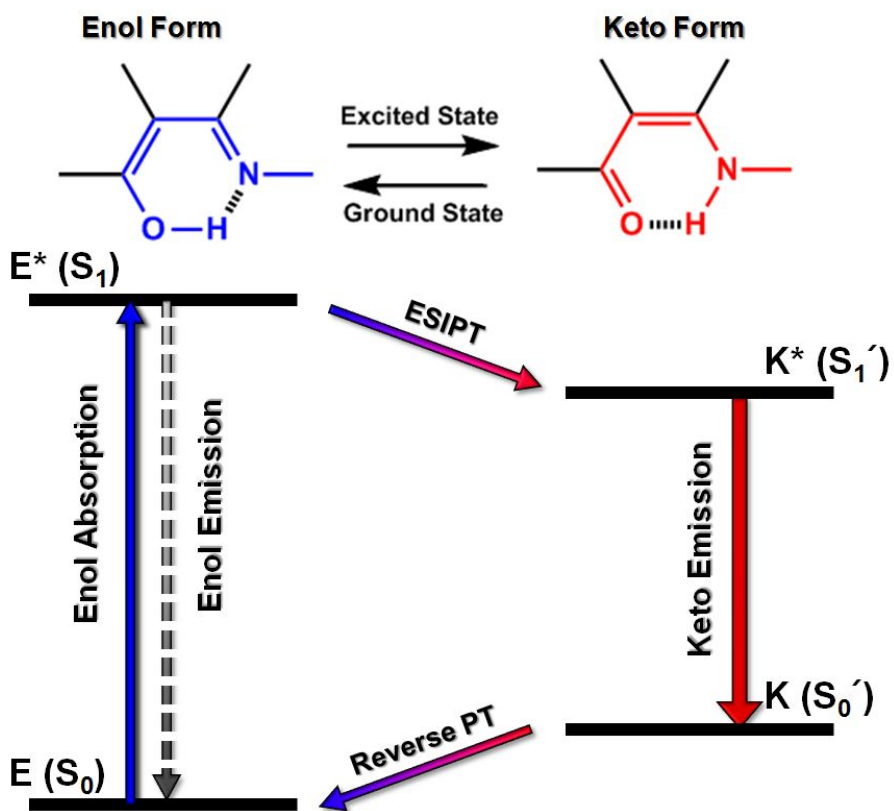


Figure 1.3 Schematic four-level energy diagram of ES IPT cycle.

exhibiting molecular structures are shown Scheme 1.1. As for practical works, the ESIPT molecules have applied as UV stabilizers,⁹ solar concentrators,¹⁰ organic lasers¹¹ and fluorescent probes.

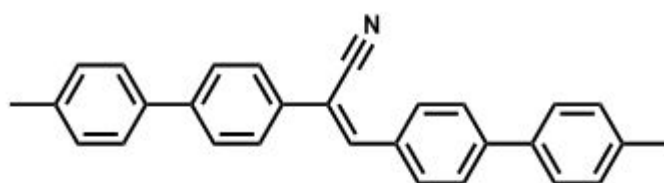
1.3 Luminescent Behavior in solid state

There have been growing interests of many scientists in highly luminescent dyes in solid-state or aggregated state. Traditional molecular structures of luminophores consist of planar conformation and extended π -conjugation. However, these organic dyes often show weak, even no fluorescence and phosphorescence in solid or aggregated state although they exhibit excellent luminescence in dilute solution state. This phenomenon is so-called “concentration quenching effect” and it is mostly attributed to enhanced non-emissive decay process in solid state, coming from strong intermolecular vibrational interactions such as exciton coupling and excimer formation. For better optoelectronic application, it is necessary to develop the dyes which efficiently radiate the luminescence in solid state.

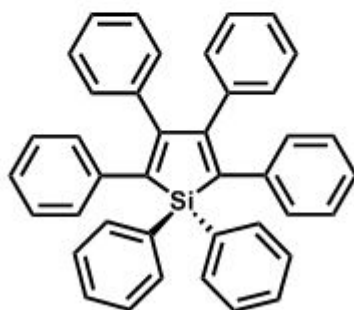
Recently, unique types of compounds showing unusual strong emission in aggregates have developed. (Figure 1.5) This unique phenomenon is named as aggregation-induced emission enhancement¹³ (AIEE) and aggregation-induced emission (AIE).¹⁴ Most of these AIEE and AIE active materials

include aromatic-ethene or aromatic silole groups.

For aromatic ethene group, for example CN-MBE,¹⁵ the enhanced emission is originated from the combination of several factors; head-to-tail J-stacking for preventing excimer formation and twist to planar conformation change. In other case, silole group, for instance HPS,¹⁶ restriction of intramolecular rotation (RIR) motion and avoidance of tight stacking in aggregated state produces the enhancement of luminescence.



CN-MBE



HPS

Scheme 1.2 Molecular structure of several aggregation-induced emission enhancement (AIEE) active dyes.

1.4 Research Objectives

Up to now, most of the researches have utilized the ESIPT fluorescence rather in dilute solution state. Even though the ESIPT molecules have advantageous emission properties, aggregated solid state fluorescence often suffer from the low quantum yield due to concentration quenching, deactivation by useless isomerization. Aiming better applications, it is highly demanded to develop new ESIPT materials with intense fluorescence in aggregated state and high-performance functionality targeting better practical application. Appropriate design of solid-state fluorescent dyes could be applied in ESIPT fluorophore. Introducing polar and bulky groups to induce J-stacking, or incorporation of bulky groups to prevent tight π - π stacking phenyl rings are representative pathways.

Herein, we demonstrate the design and synthesis of novel ESIPT molecules offering strong solid-state luminescence with beneficial applications. Firstly, elucidating the photophysical process of simple ESIPT fluorophores with enhanced fluorescence was investigated. Based on this study, we report smart-supramolecular organogel bearing fluorescent ESIPT moiety for anion detection. Moreover, triplet investigation of ESIPT dyes renders a novel mechanism for potential highly efficient blue OLED dyes. The following contents are composed of two different parts:

Chapter 2 Simple π -conjugated low molecular-weight organogelator (LMOG) showing excited-state intramolecular proton transfer (ESIPT) for anion detection.

Chapter 3 Excited-state intramolecular proton transfer (ESIPT) mediated spin up-conversion of triplet excitons toward highly efficient blue OLED devices: effect of naphthyl substitution.

1.5 References

1. Lakowicz, J. R. *Principles of Fluorescence Spectroscopy*, 3rd Ed.; Springer, 2006
2. Turro, N. J. *Modern Molecular Photochemistry*, University Science Books, Sausalito, California, 2009.
3. Valeur, B. *Molecular Fluorescence: Principles and Applications*, Wiley-VCH, Weinheim, 2001.
4. IUPAC Compendium of Chemical Terminology, 2nd Ed.; 1997.
5. M. N. Berberan-Santos and J. M. M. Garcia, *J. Am. Chem. Soc.* 1996, 118, 9391-9394.
6. J. Saltiel, H. C. Curtis, L. Metts, J. W. Miley, J. Winterle and M. Wrighton, *J. Am. Chem. Soc.* 1970, **92**, 410.
7. A. Endo, M. Ogasawara, A. Takahashi, D. Yokoyama, Y. Kato and C.

Adachi, *Adv. Mater.* **2009**, 21, 4802.

8. S. Park, O. H. Kwon, Y. S. Lee, D. J. Jang and S. Y. Park, *J. Phys. Chem. A.* **2007**, 111, 9649.

9. a) G. J. Stueber, M. Kieninger, H. Schettler, W. Busch, B. Goeller, J. Franke, H. E. A. Kramer, H. Hoier, S. Henkel, P. Fischer, H. Port, T. Hirsch, G. Rytz, J.-L. Birbaum, *J. Phys. Chem.* **1995**, 99, 10097; b) J. Keck, H. E. A. Kramer, H. Port, T. Hirsch, P. Fischer, G. J. Rytz, *J. Phys. Chem.* **1996**, 100, 14468.

10. F. Vollmer, W. J. Rettig, *J. Photochem. Photobiol. A.* **1996**, 95, 143.

11. a) A. U. Khan, M. Kasha, *Proc. Natl. Acad. Sci.* **1983**, 80, 1767; b) P. Chou, D. McMorrow, T. J. Aartsma, M. Kasha, *J. Phys. Chem.* **1984**, 88, 4596; c) S. Park, O.-H. Kwon, S. Kim, S. Park, M.-G. Choi, M. Cha, S. Y. Park and D.-J. Jang, *J. Am. Chem. Soc.* **2005**, 127, 10070.

12. a) J. Wu, W. Liu, J. Ge, H. Zhang and P. Wang, *Chem. Soc. Rev.* **2011**, 40, 3483. b) V. V. Shynkar, A. S. Klymchenko, C. Kunzelmann, G. Duportail, C. D. Muller, A. P. Demchenko, J.-M. Freyssinet and Y. Mely, *J. Am. Chem. Soc.* **2007**, 129, 2187.

13. B.-K. An, J. Gierschner and S. Y. Park, *Acc. Chem. Res.* **2011**, 45, 544.

14. Y. Hong, J. W. Y. Lam and B. Z. Tang, *Chem. Soc. Rev.* **2011**, 40,

5361.

15. B. K. An, S. K. Kwon, S. D. Jung and S. Y. Park, *J. Am. Chem. Soc.* **2002**, 124, 14410.

16. J. D. Luo, Z. L. Xie, J. W. Y. Lam, L. Cheng, H. Y. Chen, C. F. Qiu, H. S. Kwok, X. W. Zhan, Y. Q. Liu, D. B. Zhu and B. Z. Tang, *Chem. Commun.* **2001**, 1740.

Chapter 2. Simple π -conjugated Low Molecular-Weight Organogelator (LMOG) Showing Excited-state Intramolecular Proton Transfer for Anion detection

2.1 Introduction

Low molecular weight organogelators (LMOGs) are capable of being self-assembled into entangled 3-dimensional networks through non-covalent interactions such as hydrogen bonding, π - π stacking, and van der Waals force.¹ Special interests have been paid to establish LMOGs with π -conjugated structures because controlled gelation of them could afford another viable mean for fabrication of nano optoelectronic devices with exceptional ease and simplicity.² We and other groups have demonstrated fabrication of conducting nanocables³ by employing gelation of such π -conjugated LMOGs. In addition, by combining the ability of gels to respond external stimuli, enabling facile and cost-efficient construction of ‘smart devices’^{4a} such as tunable templates,^{4b} reaction vessels,^{4c} and detection kits.⁵ Since few anion such as fluoride plays important roles on human body system, “anion responsive” organogel have attracted intensive research

attention.^{4a}

Excited-state intramolecular proton transfer (ESIPT) is intramolecular tautomerization which occurs between a vicinal Brøsted acid and base moieties under photoexcitation.⁶ The proton transfer transiently produces a proton-transferred species, keto form (K) which radiates strong fluorescence emission with a large Stokes-shift. Subsequent back proton transfer restores the original species, enol form (E), completing ESIPT. Since normal fluorescence is often observed for E form, interruption of ESIPT results in spectral shifts in absorption and fluorescence.⁷ It is therefore envisioned that incorporation of ESIPT moieties in LMOGs would produce multifunctional gels that feature strong emission along with photophysical change in response to basic anion.

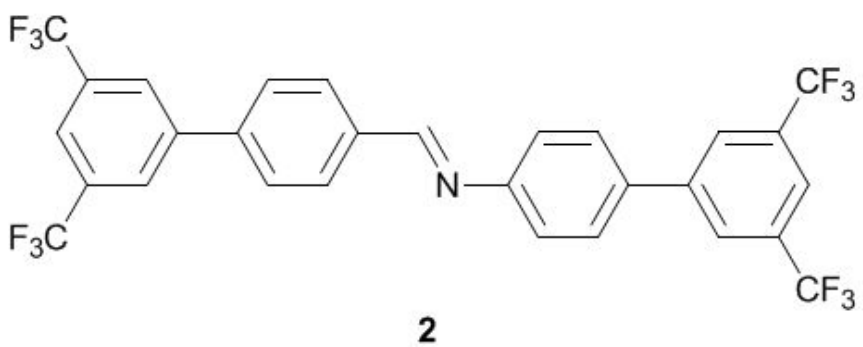
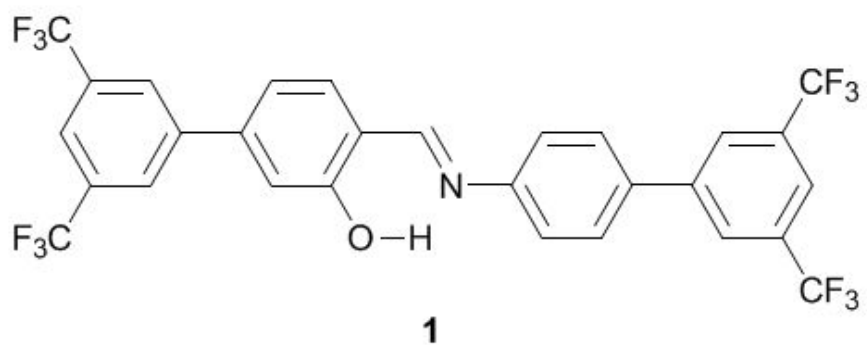
Herein, we report design and synthesis of a novel π -conjugated LMOG **1** (Scheme 2.1), which spontaneously forms entangled nanowires, bringing about to gelation. The π -conjugated organogelator comprises four trifluoromethyl (CF₃) groups which induces sliding of the molecules along the molecular axis direction to form J-aggregation for efficient fluorescence emission, provide strong hydrogen bonding of C-F \cdots H-C and offer π - π stacking force to result in 1-D self-assembled nanostructure.^{8a} Salicylidene aniline group is to serve an ESIPT chromophore with fluorescence response

toward basic anion⁹ and its hydroxyl group increases polarity of whole molecule procuring stronger anisotropic intermolecular interactions for 1-D nanoribbon formation, similar to the role of cyano group in previous report.^{8a} We expected that addition of basic anion such as fluoride ion invokes prompt collapse of the gel structures, leading to reversible sol-gel. Moreover, the sol-gel transition accompanies considerable changes in visible absorption and fluorescence properties. We underscore that π -conjugated LMOG could provide us with tuning of trimodal supramolecular photofunctionality.

2.2 Result and Discussion

2.2.1 Formation of organogel

Spontaneous gelation was observed when hot 1,2-dichloroethane, 1-octanol, 1-heptanol, and 1,1,2,2-tetrachloroethane solutions of **1** (2.0-3.0 wt %) were cooled down to room temperature (Figure 2.1). The ‘drop-ball’ technique was employed to determine gel-to-sol transition temperature (T_{gel}),¹⁰ being 44-55 °C. The prepared organogel is stable over months. The organogel of **1** consists of entangled ribbons with several tens μm thickness as revealed by optical microscope and field-emission scanning electron microscope (FE SEM) images (Figure 2.1).



Scheme 2.1 Chemical structure of organogelator, **1** and control compound, **2**

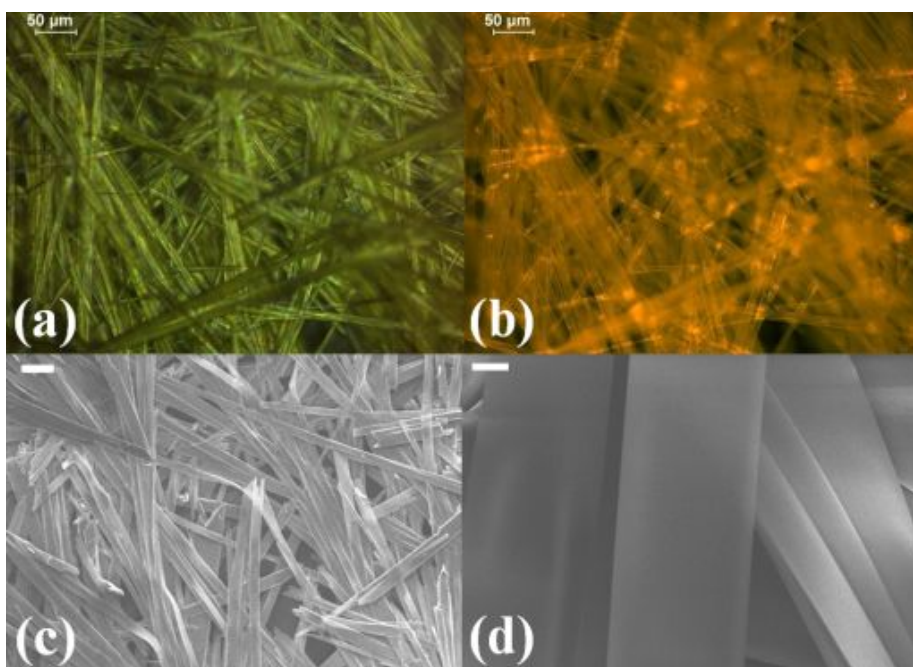


Figure 2.1 (a) Optical and (b) fluorescence ($\lambda_{\text{ex}} = 365 \text{ nm}$) microscope images of xerogel of **1** casted on a glass substrate. FE-SEM images of xerogel of **1** under 15.0 kV. The scale bar indicates (c) 50 μm and (d) 5 μm .

2.2.2 Gelated induced Enhanced Emission (GIEE) behavior and their supramolecular structure of 1

UV-Vis absorption and photoluminescence spectra indicate J-type aggregation for construction of the ribbons. In fact, a new absorption band at 420 nm band, which is significantly red-shifted from the normal π - π^* absorption band (363 nm), was observed upon gelation (Figure 2.2). The gelation also accompanied a 24-fold enhancement in fluorescence intensity (Figure 2.3). These spectral features are strong indication of J-aggregate formation of π -conjugated molecules as reported earlier.¹¹ In addition, the optical changes are accordance with previous reports for aggregation of salicylideneaniline-based molecules.¹²

We have analysed the out of plane X-ray diffraction (XRD) pattern of xerogel of 1. The XRD pattern is characterized with strong diffraction at 11.43 ° ($d_{100} = 7.75 \text{ \AA}$) and its higher order diffractions at 22.92, 34.64, and 46.76 ° (Figure 2.4). By comparison with quantum chemically optimized molecular length of 1 (21.29 Å, Figure 2.4b; DFT B3LYP/6-31G (d,p)), the aggregation superstructure envisaged to be the lamellar structure of 1 with a tilt angle of 21.6 °. It should be underscored that this tilt arrangement is in accordance with the J-aggregation which is inferred from UV-Vis absorption and fluorescence spectra. We further obtained wide angle X-ray scattering

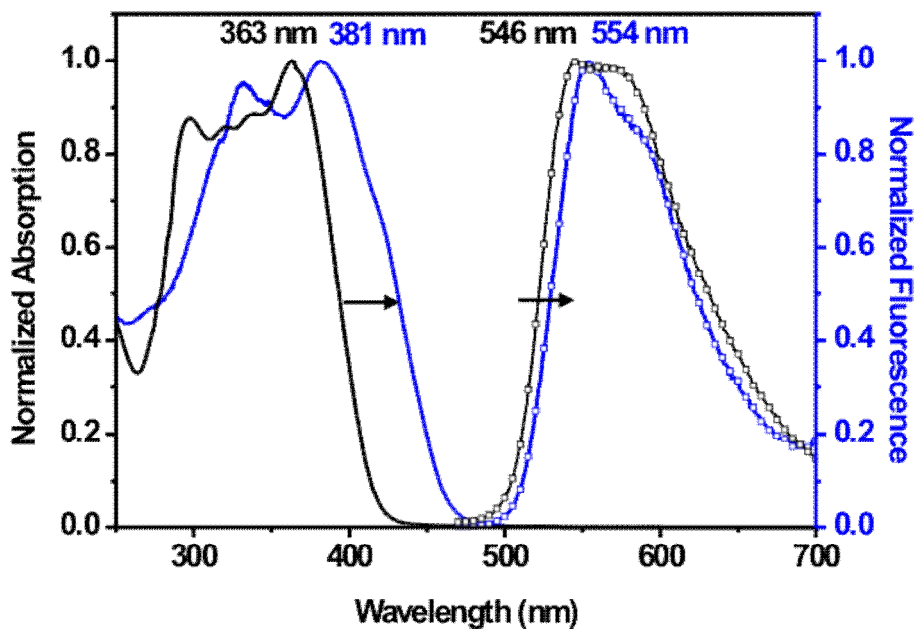


Figure 2.2 Comparison of normalized UV-Vis absorption (solid) and fluorescence (solid-dot) spectra of **1** solution (black; 10 μM , 1,2-dichloroethane) and xerogel (blue; 0.1 wt % in sodium chloride solid solution). Diffuse reflectance technique was employed for the measurement of the UV-vis absorption spectrum (corrected by Kubelka-Munk function).

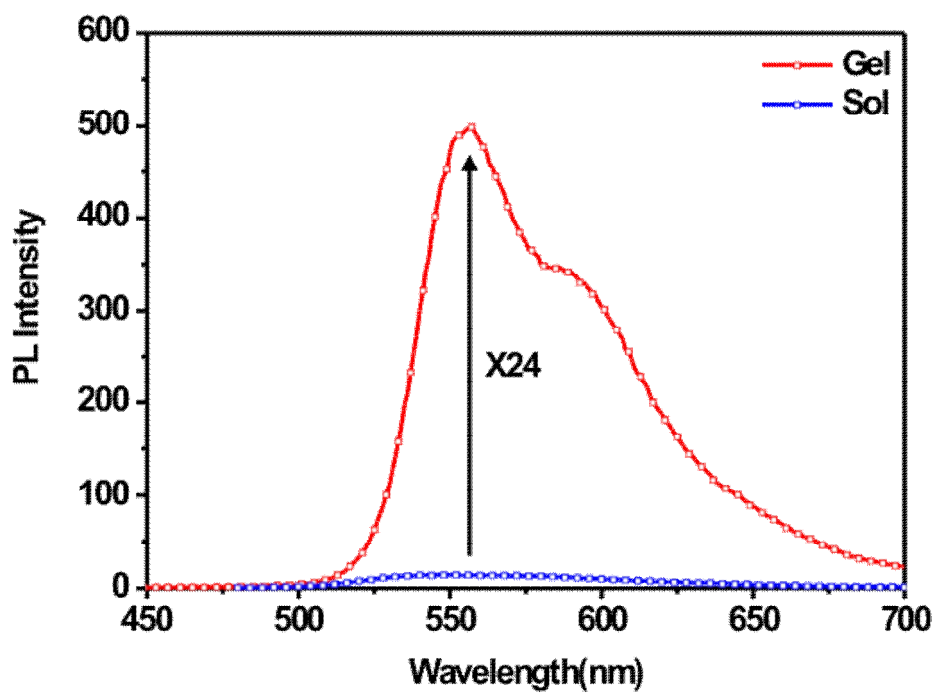


Figure 2.3 Fluorescence spectrum of **1** with concentration of 2.0 wt% in 1,2-dichloroethane hot solution (blue) and after gelation

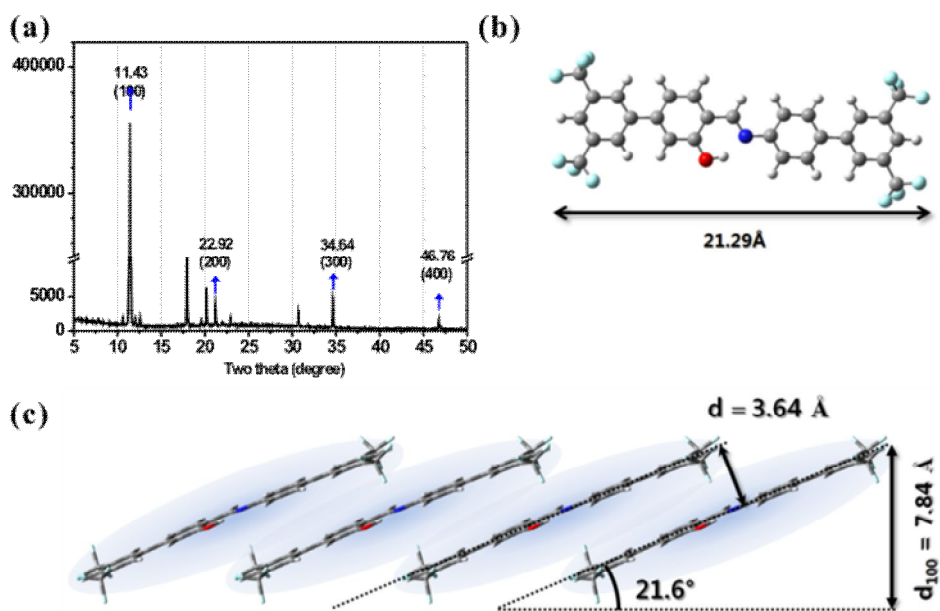


Figure 2.4 (a) XRD profile of xerogel **1**. (b) Optimized molecular length of **1** from quantum chemical calculations with Gaussian 09 software package (c) Suggested packing structure of **1** in gel state.

(WAXS) patterns which comprise strong peaks at d spacing of 7.84, 4.95, 4.38, and 3.64 Å (Figure 2.5). Importantly, the d spacing of 3.64 Å is in agreement with the typical π - π stacking distance,¹³ indicating that the π - π interaction plays a significant role on the gelation. In addition to the π - π interaction, several other factors contribute to the spontaneous J-aggregate formation. We previously suggested^{8a} that CF₃ groups aid strong intermolecular interaction by donating C-F...H-C hydrogen bonding, while their bulky nature induces 'sliding-away' disposition between molecular planes. More importantly, the presence of the polar hydroxyl group increase polarity from 1.55 D of **2** to 2.28 D of **1** (Figure 2.6, calculated with Gaussian 09 software) resulting stronger anisotropic intermolecular interaction between neighboring molecule. In fact, **2** that lacks hydroxyl group did not form organogel under the gelation condition of **1** (Figure 2.7). This observation suggests a crucial role of the ES IPT group in gelation. Taken together, the gelation with the unique J-type lamellar arrangement can be ascribed to balanced combination of the π - π interaction, the C-F...H-C interaction, the steric effect, and the dipolar interaction due to the hydroxyl group.

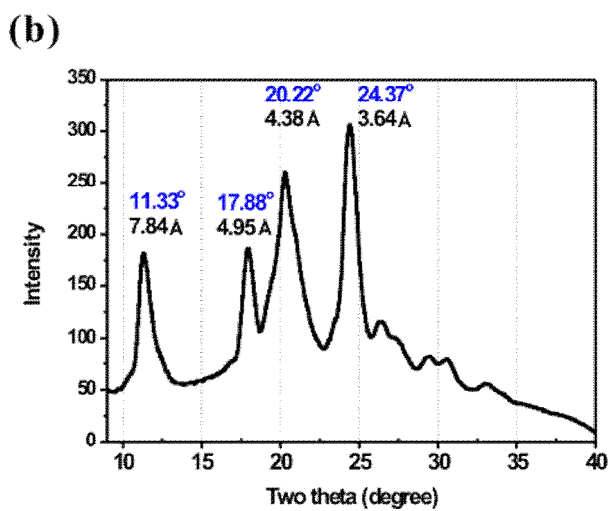
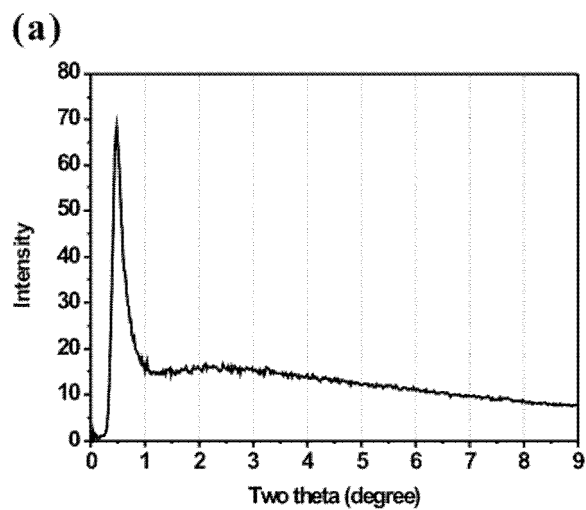


Figure 2.5 (a) Small angle X-ray scattering (SAXS) and (b) Wide angle X-ray scattering (WAXS) profiles of xerogel **1** casted on glass substrate.

Electronic potential isosurface
-1.600E-2  +1.600E-2

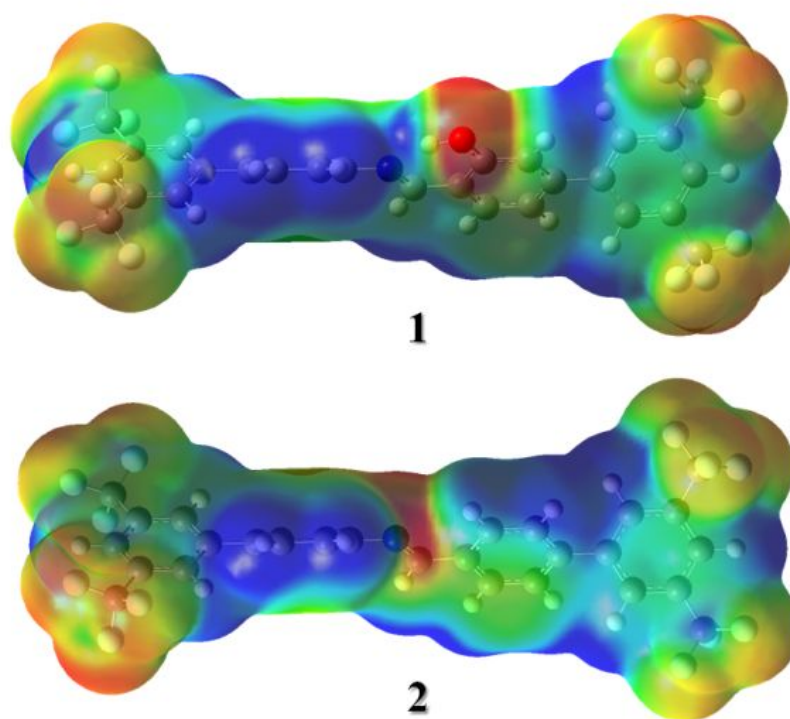


Figure 2.6 Electrostatic potential isosurfaces of **1** and **2**. Gaussian 09 software package was employed for the quantum chemical calculations. Potential ranges were set to constant value from -1.600E-2 to +1.600E-2.

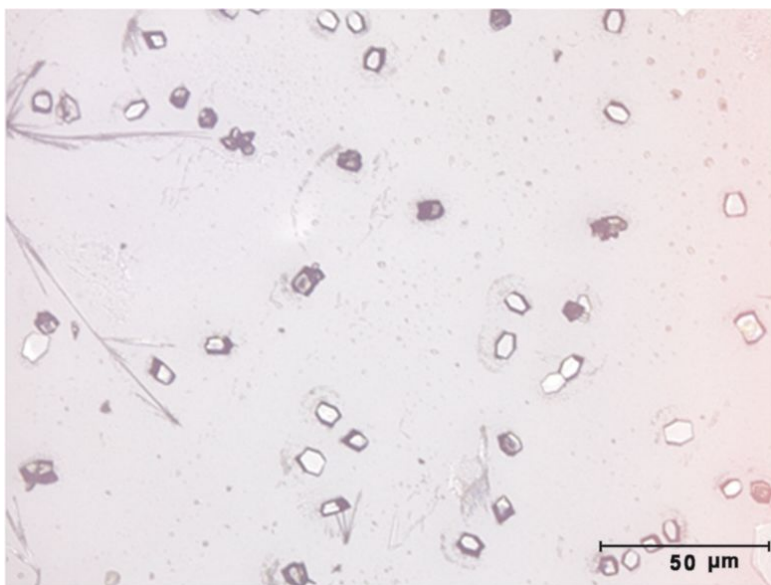


Figure 2.7 Image of drop-casted film (2.0 wt% in 1,2-dichloroethane) of **2**.

2.2.3 Anion-responsive behavior of supramolecular organogel

Having understood the gelation behavior, we sought to apply this property to demonstration of a stimuli-responsive smart gel. We anticipated that fluoride anion might destroy the organogel by deprotonation of the hydroxyl group and by disrupting the C-F...H-C interaction. As expected, an addition of Bu₄NF to organogel (2.0 wt % in 1,2-dichloroethane) leads to gel-to-sol transition at the interface between TBAF powder and organogel. (Figure 2.8c) Slow diffusion of sol region induces total collapse of organogel, completing gel-to-sol transition. The transition accompanies huge changes in absorption and fluorescence spectra (Figure 2.9). The gel-to-sol transition is highly selective to fluoride ion because other anions, such as halide ions and nitrite and cyanide, do not promote such change (Acetate ion induces the identical gel-to-sol transition, but the extent of the transition is much smaller than the case of fluoride ion see figure 2.10). It should be specially noted that the gel-sol transition is reversible since the addition of CH₃OH (10 wt %) followed by the heating-cooling cycle restores the organogel (Figure 2.8i).

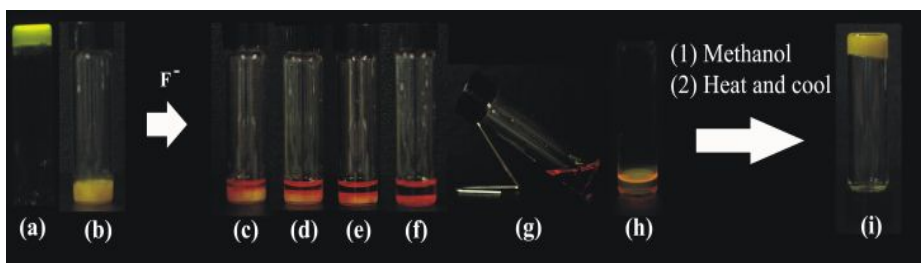


Figure 2.8 Fluoride ion induces collapse of organogel formed in 1,2-dichloroethane (2.0 wt %, 1.00 g): (a) fluorescence emission of as-prepared organogel under photoexcitation at 365 nm; (b) absorption colour of as-prepared organogel; (c) (f) time course of the collapse of organogel by TBAF, (c) 0 min, (d) 10 min, (e) 20 min, (f) 30 min; (g) fully collapsed organogel, (h) collapsed organogel under photoexcitation at 365 nm; (i) after addition of 0.1 mL of methanol and then heated and cooled to re-form organogel.

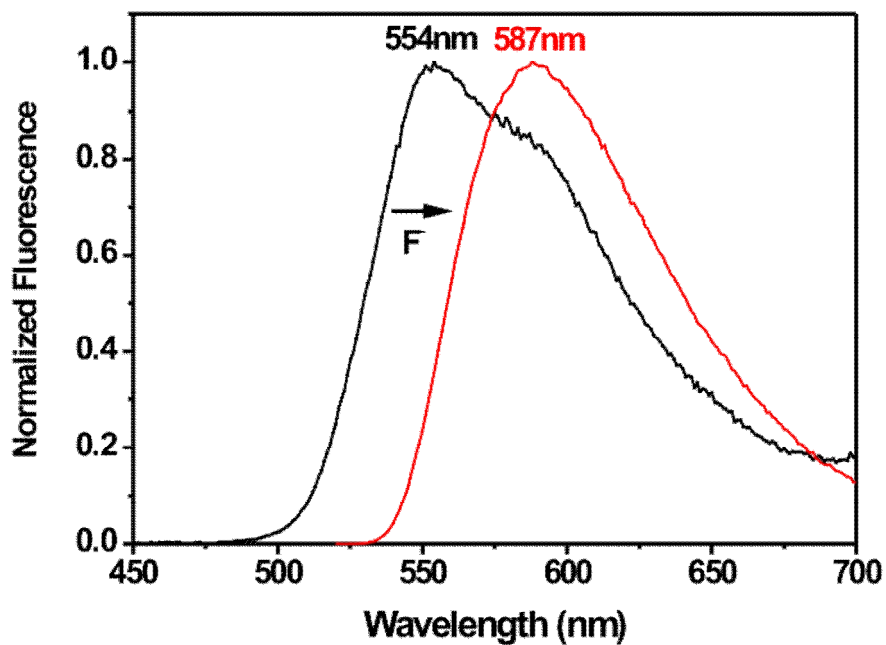


Figure 2.9 Fluorescence spectrum of (black) organogel of **1** (1,2-dichloroethane) and (red) 30 minutes after addition of TBAF.

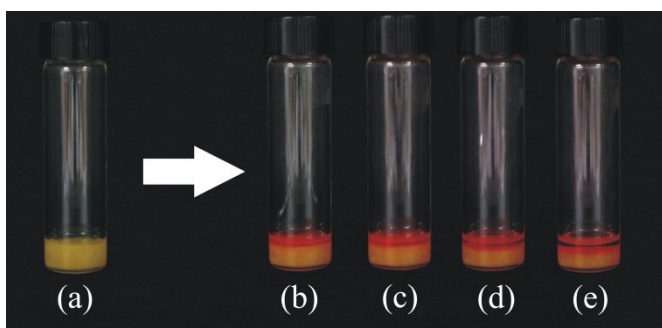


Figure 2.10 Acetate ion induces collapse of organogel **1** formed in 1,2-dichloroethane (2.0 wt %, 1.00 g): time course of the collapse of organogel by TBAF, (a) 0 min, (b) 10 min, (c) 20 min, (d) 30 min and (e) 40 min.

2.2.4 Origin of anion-responsive behavior

The origin of gel-to-sol could be elucidated by understanding of special interaction between **1** and fluoride ion in gel interface at individual molecule level. Hence, we investigated photophysical properties in isolated solution state, which could be measured and similar to that of gelated state. **1** in solution state displayed strong absorption band of 363 nm (Figure 2.11a) coming from π - π^* transition as well as 180 nm of large Stokes shifted yellow fluorescence emission ($\lambda_{\text{max}} = 546$ nm, $\Phi = 0.0042$) (Figure 2.11b). These properties are in close resemblance with that of gelated state. (absorption $\lambda_{\text{max}} = 381$ nm, fluorescence $\lambda_{\text{max}} = 554$ nm, Figure 2.2). Addition of tetrabutylammonium fluoride (TBAF) standard solution into 10 μM THF solution of **1** brings about gradual decrease of 364 nm absorption and 540 nm emission bands. Simultaneously, new absorption ($\lambda_{\text{max}} = 481$ nm) and emission ($\lambda_{\text{max}} = 602$ nm, $\Phi = 0.025$) bands came around (Figure 2.11a, b) with binding constant of 3.59×10^3 (Figure 2.12). The origin of the new bands seems to be intramolecular charge transfer (ICT) absorption and emission (Figure 2.11c) of deprotonated **1** by NMR titration with fluoride ion. We could observe both disappearance of the 13.3 ppm hydroxyl peak in ^1H NMR (Figure 2.13) as well as appearance of the -155.33 ppm¹⁴ HF_2^- in ^{19}F NMR (Figure 2.14). At the same time, chemical shifts of protons from

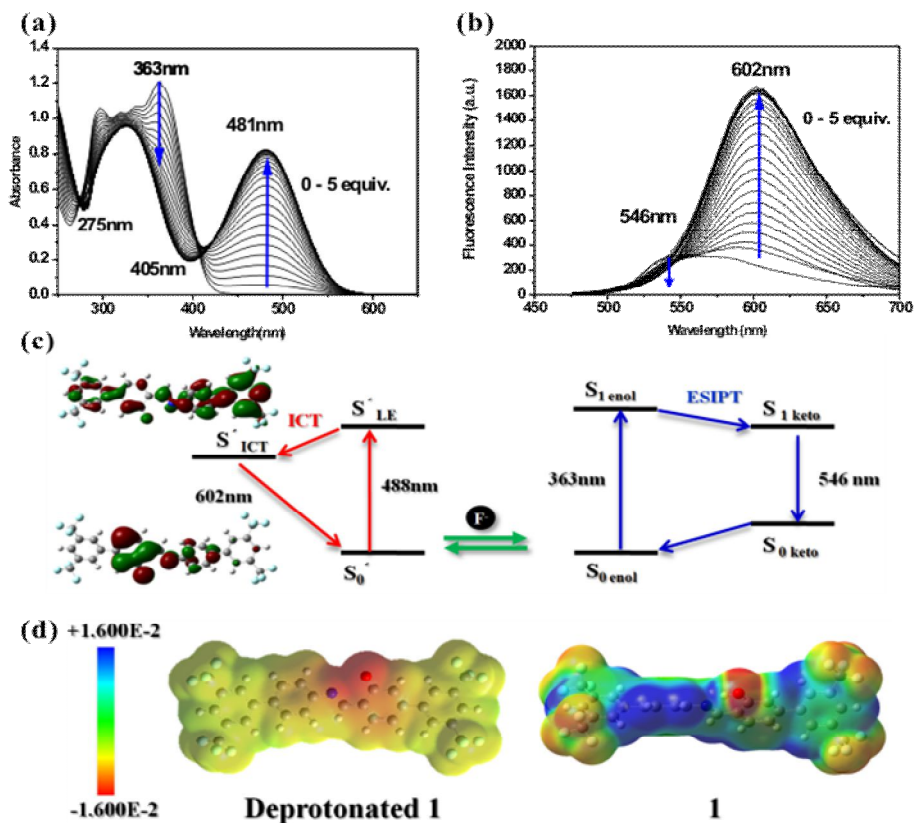


Figure 2.11 (a) UV-vis absorption and (b) fluorescence ($\lambda_{\text{ex}} = 405 \text{ nm}$) spectral change of **1** ($40 \mu\text{M}$ in THF) with the addition of tetrabutylammonium fluoride (TBAF) solution from 0 equiv. to 5 equiv. by 0.2 equiv. (c) Schematic representation of a mechanism for fluorescence change of **1** in response to fluoride ion. (d) Electrostatic potential isosurfaces of deprotonated **1** and **1**. Gaussian 09 software package was employed for the quantum chemical calculations.

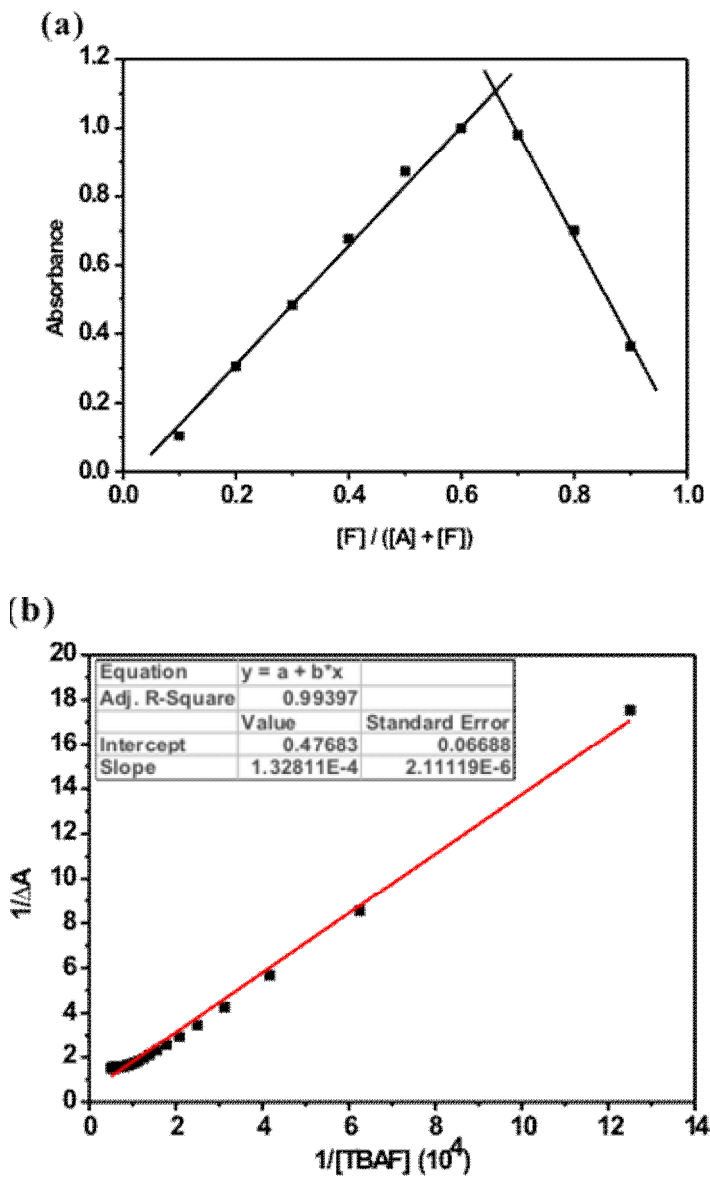


Figure 2.12 (a) Job's plot utilizing the absorbance at 481 nm. The total ion concentration $[F] + [1] = 100 \mu\text{M}$ (b) Benesi-Hildebrand plot by utilizing absorbance at 365 nm.

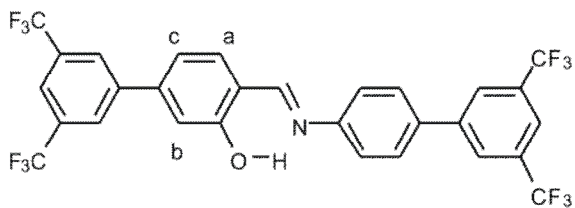
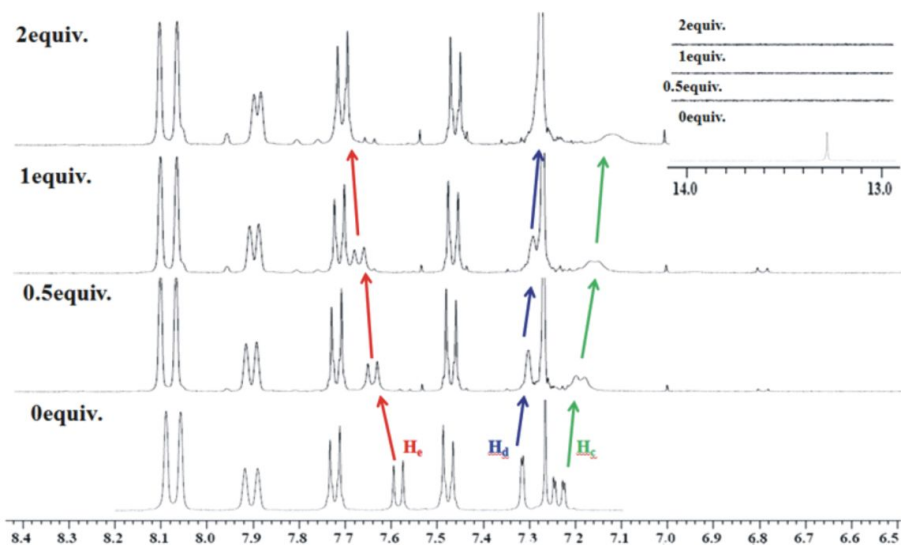


Figure 2.13 1H NMR titration of 1.0 mM of **1** and specific concentration of TBAF.

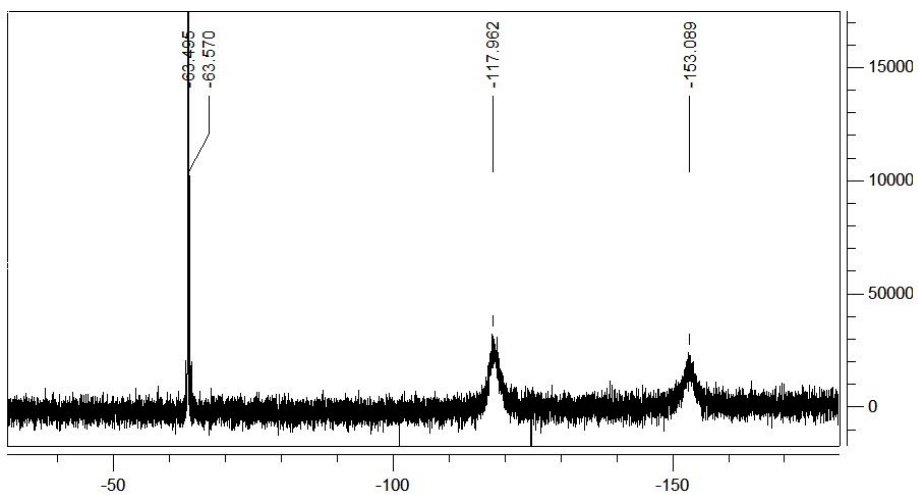


Figure 2.14 ^{19}F NMR spectra from mixture of 1.0 mM of **1** and 1.0 mM of TBAF. -63.50 ppm and -63.57 ppm indicates two trifluoromethyl groups, -117.96 ppm indicates tetrabutylammonium fluoride salts and -153.09 ppm indicates HF_2^- anion.

salicylaldehyde rings slightly shifted to up-field for two protons in salicylic ring and to downfield for other protons due to their electron density change caused by deprotonation.⁷ Similar results was observed from the titration of tetrabutylammonium hydroxide. Clearly, it is confirmed that fluoride ion-induced collapse of the gel was triggered by deprotonation of hydroxyl group at organogel interface as same as that in solution state. It could be explained that basic anion such as acetate could act as a weaker base,¹⁵ so the acetate ion also induces similar gel collapse but smaller amount.

Taken together, **1** molecule acts as a fluoride sensor in solution state. Moreover, the anion responsibility remains as the solution state even **1** molecule is incorporated in gelled state. The locked dihedral motion of the ESIPT moiety is liberated due to the loss of the intramolecular hydrogen bonding. In addition, negative charge imposed on the ESIPT unit (Figure 2.11d) generates repulsive interactions between adjacent molecules. The main gelation driving force from appropriate combination of π - π stacking force, dipole and C-F \cdots H-C interaction, as discussed before, is hindered. Thus, the mechanism for collapse of gel is reasonably described by these effects. Fluoride ion-promoted rupture accompanies loss of original absorption color and ESIPT fluorescence, as clearly shown in Figure 2.11.

2.3 Conclusion

To summarize, we designed and synthesized a π -conjugated organogelator **1** comprising the CF₃ groups and the ESIPT moiety. **1** spontaneously forms organogel which are characterized with the J-type molecular arrangement, which stems from combined effects of π - π interaction, the C-F \cdots H-C interaction, stronger dipole moment, and the dipolar interaction. The selective interaction with fluoride ions promptly destroys the organogel, affording huge optical changes in absorption and fluorescence. The sol-gel transition is reversible as demonstrated by CH₃OH-induced gelation. Photophysical investigations suggest the mechanism underlying the reversible sol-gel transition, which involves reversible deprotonation.

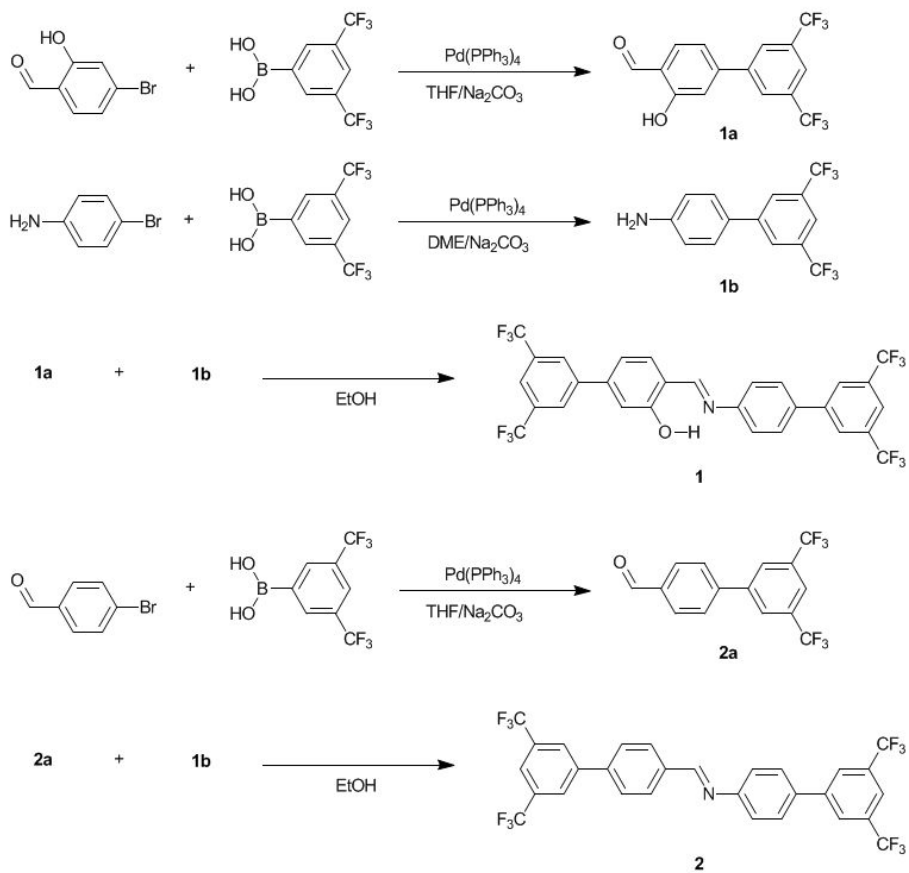
2.4 Experimental

2.4.1 General Information

Commercially available 4-bromo-2-hydroxybenzaldehyde, 4-bromoaniline, 4-bromobenzaldehyde, 3,5-bis(trifluoromethyl) phenylboronic acid, *Tetrakis*(triphenylphosphine)palladium(0) and all kinds of solvent were purchased from Sigma Aldrich Chemical Co. and used without further purification. ^1H NMR were measured with a Bruker-300 spectrometer and ^{13}C NMR were measured with a Bruker-500 using chloroform-d as a solvent with tetramethylsilane as the internal. High resolution mass spectroscopy (HRMS) was investigated with a JEOL JMS-700. Elemental analysis was measured with an EA1112 (CE Instrument, Italy). Steady state absorbance, fluorescence excitation and emission spectra were recorded in an Uvikon 933 (Kontron) and a Fluoromax 3 (Jobin Yvon Horiba) with concentration of the solute 10 μM . Each fluorescence spectrum was corrected by detector sensitivity and distracted by baseline. Solid state of UV-reflection absorbance and emission spectra were recorded in a Cary5000 (Varian). Sodium chloride is purchased from SDS and dried over 3 days under 100°C. XRD measurements were performed with a model of D8-Advance (Bruker), (CuK_{α} , $\lambda = 1.5418 \text{ \AA}$). Relative quantum yield was calculated by using

quinine sulfate in 0.5 M sulfuric acid as fluorescence reference standard ($\Phi = 0.546$). Gaussian 09 and GaussView 5.0 have been employed for quantum chemical drawing and calculation. The geometry of the ground-state structures were optimized by the density functional theory using the hybrid B3LYP functional with the split-valence polarized 6-31g (d,p) basis set for all species. To obtain estimates of the vertical electronic excitation energies that include some account of electron correlation, time-dependent density functional theory (TD-DFT) calculations with the B3LYP functional and 6-31g (d,p) basis set were utilized. B3LYP corresponds to the combination of Becke's three parameter exchange functional (B3) with a Lee-Yang-Parr fit for the correlation functional (LYP).

Overall synthetic routes are illustrated in Scheme 2.2 and detailed synthetic procedures are shown.



Scheme 2.2 Overall synthetic routes to **1** and **2**.

2.4.2 Synthesis

3-hydroxy-3',5'-bis(trifluoromethyl)biphenyl-4-carbaldehyde (1a) : 4-bromo-2-hydroxybenzaldehyde 0.53 g (2.64 mmol), 3,5-bis(trifluoromethyl)phenylboronic acid 0.82 g (3.16 mmol) and Pd(PPh₃)₄ 0.15 g (0.13 mmol) were added in 30 mL tetrahydrofuran solution in dark condition. Then, 15 mL of aqueous sodium carbonate 2.0 M solution was added. Reaction mixtures were vigorously stirred and reflux. After 18 hours, reaction mixtures turned to black solution. The crude mixture was poured into distilled water and titrated to pH 7.0 with 1.0 M hydrochloric acid. Organic layer was extracted by 150 mL of dichloromethane 3 times. The solution obtained was dried with rotary evaporator and was purified by silica column chromatography with (ethyl acetate: n-hexane = 1:30) solution as an eluent. After drying eluent, white powder of 1.12 g was gained (Yield = 79.3%). ¹H NMR (300 MHz, CDCl₃, 298 K, ppm) δ = 11.14 (s, 1H), 9.98 (s, 1H), 8.04 (s, 2H), 7.94 (s, 1H), 7.71 (d, 1H, 7.92 Hz), 7.28~7.24 (m, 2H). ¹³C NMR (125 MHz, CDCl₃, 298 K, ppm) δ = 196.30, 162.24, 146.53, 141.76, 134.78, 127.71, 125.17, 122.63, 122.56, 122.53, 121.55, 120.66, 116.65. HRMS (EI, positive): calc. for C₁₅H₉F₆O₂ [M+H]⁺ 334.0462; found 334.0503. Elemental analysis: calc. for C 53.91, H 2.41, O 9.57; found: C 53.97, H 2.36, O 9.96.

3',5'-bis(trifluoromethyl)biphenyl-4-amine (1b) : 3,5-bis(trifluoromethyl)phenylboronic acid 0.90 g (3.49 mmol) and Pd(PPh₃)₄ 0.17 g (0.14 mmol) were added 3 times to solution of 4-bromoaniline 1.50 g (2.64 mmol) in 30 mL dimethylether solution with 15 mL aqueous 2.0 M sodium carbonate solution. Reaction mixtures were vigorously stirred and reflux. After 18 hours, solution became black solution. The crude mixture was poured into distilled water and titrated to pH 7.0 with 1.0 M hydrochloric acid. Organic layer was extracted by 150 mL of dichloromethane 3 times. The solution obtained was dried with rotary evaporator and was purified by silica column chromatography with (ethyl acetate: n-hexane = 1:5) solution as an eluent. After drying eluent, white powder of 0.70 g was gained (Yield = 46.9%). ¹H NMR (300 MHz, CDCl₃, 298 K, ppm) δ = 7.94 (s, 2H), 7.75 (s, 1H), 7.44 (d, 2H, 8.5 Hz), 6.79 (d, 2H, 8.5 Hz), 3.95 (s, 1H). ¹³C NMR (125 MHz, CDCl₃, 298K, ppm) δ = 147.30, 143.18, 132.13, 131.70, 128.21, 128.15, 126.15, 125.34, 121.72, 119.65, 116.71, 115.48. HRMS (EI, positive): calc. for C₁₄H₉F₆N [M]⁺ 305.0639; found 305.0642. Elemental analysis: calc. for C 55.09, H 2.97, N 4.59; found C 55.45, H 2.90, N 4.65.

(E)-4-((3',5'-bis(trifluoromethyl)biphenyl-4-ylimino)methyl)-3',5'-

bis(trifluoromethyl)biphenyl-3-ol (1) : The solution of 3-hydroxy-3',5'-bis(trifluoromethyl)biphenyl-4-carbaldehyde 0.70g (1a, 2.09 mmol) and 3',5'-bis(trifluoromethyl)biphenyl-4-amine 0.64 g (1b, 2.09 mmol) in 50 mL of ethanol was refluxed. After 24 hours, the crude solutions were cool down for 0 °C. Obtained solution was filtered off and residue was recrystallized in 50 mL hot ethanol. After Filtering, yellowish needle shape powder of 1.08 g was gained (Yield = 82.8%). ¹H NMR (400 MHz, CDCl₃, 298 K, ppm) δ = 13.31 (s, 1H), 8.76 (s, 1H), 8.09 (d, 4H, 12.5 Hz), 7.91 (d, 2H), 7.72 (d, 2H, 8.5 Hz), 7.58 (d, 2H, 8.2 Hz), 7.48 (d, 2H, 8.2 Hz), 7.32 (d, 1H, 1.5 Hz), 7.25 (dd, 1H, 7.9 Hz, 1.5 Hz). ¹³C NMR (125 MHz, CDCl₃, 298K, ppm) δ = 160.06, 152.56, 142.90, 142.57, 141.32, 136.66, 136.24, 130.03, 128.36, 127.92, 127.50, 127.42, 125.42, 125.32, 122.08, 121.81, 121.71, 121.06. HRMS (FAB, positive): calc. for C₂₉H₁₆F₁₂NO [M+H]⁺ 621.1040; found 622.1042. Elemental analysis: calc. for C 56.05, H 2.43, O 2.57, N 2.25; found C 56.06, H 2.33, O 2.89, N 2.27.

3',5'-bis(trifluoromethyl)biphenyl-4-carbaldehyde (2a) : 4-bromobenzaldehyde 0.90 g (4.86 mmol), 3,5-bis(trifluoromethyl)phenylboronic acid 1.51 g (5.84 mmol) and Pd(PPh₃)₄

0.28 g (0.24 mmol) were added in 30 mL tetrahydrofuran solution in dark condition. Then, 15 mL of aqueous sodium carbonate 2.0 M solution was added. Reaction mixtures were vigorously stirred and reflux. After 18 hours, reaction turns to black solution. The crude mixture was poured into distilled water and titrated to pH 7.0 with 1.0 M hydrochloric acid. Organic layer was extracted by 150 mL of dichloromethane 3 times. The solution obtained was dried with rotary evaporator and was purified by silica column chromatography with (ethyl acetate: n-hexane = 1:30) solution as an eluent. After drying eluent, white powder of 1.49 g was gained (Yield = 96.3%). ¹H NMR (300 MHz, CDCl₃, 298 K, ppm) δ = 10.40 (s, 1H), 8.05 (s, 2H), 8.03 (d, 2H), 7.93 (s, 1H), 7.79 (d, 2H). ¹³C NMR (125 MHz, CDCl₃, 298K, ppm) δ = 191.68, 144.07, 142.16, 136.61, 132.88, 130.78, 128.21, 127.69, 124.51, 122.25. HRMS (CI, positive): calc. for C₁₅H₉F₆O [M]⁺ 319.0558; found 319.0557. Elemental analysis: calc. for C 56.62, H 2.53, O 5.03; found C 56.66, H 2.47, O 5.13.

(E)-N-((3',5'-bis(trifluoromethyl)biphenyl-4-yl)methylene)-3',5'-

bis(trifluoromethyl)biphenyl-4-amine (2) : The solution of 3',5'-bis(trifluoromethyl)biphenyl-4-carbaldehyde 0.63 g (2a, 1.96 mmol) and 3',5'-bis(trifluoromethyl) biphenyl-4-amine 0.60 g (1b, 1.96 mmol) in 50 mL

of ethanol was refluxed. After 24 hours, the crude solutions were cool down for 0 °C. Obtained solution was filtered off and residue was recrystallized in 50mL hot ethanol. After Filtering, white powder of 0.77 g was gained (Yield = 65.1%). ¹H NMR (300 MHz, CDCl₃, 298 K, ppm) δ = 8.58 (s, 1H), 8.07 (m, 6H), 7.89 (d, 1H, 15.2 Hz), 7.75 (d, 2H, 8.3 Hz), 7.69 (d, 2H, 8.4 Hz), 7.39 (d, 2H, 8.4 Hz). ¹³C NMR (125 MHz, CDCl₃, 298 K, ppm) δ = 162.61, 161.93, 148.97, 143.12, 142.58, 142.36, 137.23, 133.51, 128.63, 122.40, 119.51, 118.28, 116.27. HRMS (FAB, positive): calc. for C₂₉H₁₆F₁₂N [M]⁺ 606.1091; found 606.1089. Elemental Analysis: calc. for C 57.53, H 2.50, N 2.31; found C 57.57, H 2.50, N 2.31.

2.5 References

1. (a) L. A. Estroff and A. D. Hamilton, *Chem. Rev.*, 2004, **104**, 1201; (b) N. M. Sangeetha and U. Maitra, *Chem. Soc. Rev.*, 2005, **34**, 821; (c) M. George and R. G. Weiss, *Acc. Chem. Res.*, 2006, **39**, 489.
2. A. L. Briseno, S. C. B. Mannsfeld, S. A. Jenekhe, Z. Bao and Y. Xia, *Mater. Today*, 2008, **11**, 38.
3. (a) J. H. Kim, Y. Jung, J. W. Chung, B.-K. An and S. Y. Park, *Small*, 2009, **5**, 804; (b) L. Jiang, H. Dong and W. Hu, *Soft Matter*, 2011, **7**, 1615.
4. (a) M.-O. M. Piepenbrock, G. O. Lloyd, N. Clarke and J. W. Steed,

Chem. Rev., 2010, **110**, 1960; (b) J. A. Foster, M. Piepenbrock Marc-Oliver, G. O. Lloyd, N. Clarke, A. K. Howard Judith and J. W. Steed, *Nat. Chem.*, 2010, **2**, 1037; (c) D. Diaz Diaz, D. Kuhbeck and R. J. Koopmans, *Chem. Soc. Rev.*, 2011, **40**, 427.

5. (a) Q. Liu, Y. Wang, W. Li and L. Wu, *Langmuir*, 2007, **23**, 8217; (b) C. Wang, D. Zhang and D. Zhu, *Langmuir*, 2007, **23**, 1478; (c) H. Yang, T. Yi, Z. Zhou, Y. Zhou, J. Wu, M. Xu, F. Li and C. Huang, *Langmuir*, 2007, **23**, 8224; (d) M. Teng, G. Kuang, X. Jia, M. Gao, Y. Li and Y. Wei, *J. Mat. Chem.*, 2009, **19**, 5648; (e) Y.-M. Zhang, Q. Lin, T.-B. Wei, X.-P. Qin and Y. Li, *Chem. Commun.*, 2009, 6074; (f) J.-W. Liu, Y. Yang, C.-F. Chen and J.-T. Ma, *Langmuir*, 2010, **26**, 9040.

6. (a) J. E. Kwon and S. Y. Park, *Adv. Mater.*, 2011, **23**, 3615; (b) J. Wu, W. Liu, J. Ge, H. Zhang and P. Wang, *Chem. Soc. Rev.*, 2011, **40**, 3483; (c) S. Park, S. Kim, J. Seo and S. Y. Park, *Macromol. Res.*, 2008, **16**, 385.

7. (a) X. Peng, Y. Wu, J. Fan, M. Tian and K. Han, *J. Org. Chem.*, 2005, **70**, 10524; (b) Y. Wu, X. Peng, J. Fan, S. Gao, M. Tian, J. Zhao and S. Sun, *J. Org. Chem.*, 2007, **72**, 62; (c) C. Qinghui, D. A. Medvetz and P. Yi, *Chem. Mater.*, 2007, **19**, 6421; (d) M. K. Nayak, J. Seo, S. Park and S. Y. Park, *J. Photochem. Photobiol., A*, 2007, **191**, 228.

8. (a) B. K. An, D. S. Lee, J. S. Lee, Y. S. Park, H. S. Song and S. Y.

- Park, *J. Am. Chem. Soc.*, 2004, **126**, 10232; (b) B. K. An, S. H. Gihm, J. W. Chung, C. R. Park, S. K. Kwon and S. Y. Park, *J. Am. Chem. Soc.*, 2009, **131**, 3950; (c) B.-K. An, J. Gierschner and S. Y. Park, *Acc. Chem. Res.*, 2012, **45**, 544.
9. (a) S. Devaraj, D. Saravanakumar and M. Kandaswamy, *Supramol. Chem.*, 2009, **21**, 717; (b) Y. M. Hijji, B. Barare, A. P. Kennedy and R. Butcher, *Sens. Actuators, B*, 2009, **136**, 297; (c) R. Sivakumar, V. Reena, N. Ananthi, M. Babu, S. Anandan and S. Velmathi, *Spectrochim. Acta, Part A*, 2010, **75**, 1146.
10. A. Takahashi, M. Masato, T. Kato, *Polym. J.*, **1980**, 12, 335.
11. (a) H. Auweter, H. Haberkorn, W. Heckmann, D. Horn, E. Lüddecke, J. Rieger and H. Weiss, *Angew. Chem. Int. Ed.*, **1999**, 38, 2188; (b) B.-K. An, S.-K. Kwon, S.-D. Jung and S. Y. Park, *J. Am. Chem. Soc.*, **2002**, 124, 14410.
12. (a) S. Li, L. He, F. Xiong, Y. Li and G. Yang, *J. Phys. Chem. B*, **2004**, 108, 10887; (b) P. Xue, R. Lu, G. Chen, Y. Zhang, H. Nomoto, M. Takafuji and H. Ihara, *Chem. Eur. J.*, **2007**, 13, 8231.
13. R. Xu, W. B. Schweizer and H. Frauenrath, *J. Am. Chem. Soc.*, **2008**, 130, 11437.
14. S. O. Kang, D. Powell, V. W. Day and K. Bowman-James, *Angew.*

Chem. Int. Ed., **2006**, 45, 1921.

15. V. Amendola, D. Esteban-Gómez, L. Fabbrizzi and M. Licchelli, *Acc.*

Chem. Res., **2006**, 39, 343.

Chapter 3. Excited-state Intramolecular Proton Transfer (ESIPT) Mediated Spin Up-conversion of Triplet Excitons toward Highly Efficient Blue OLED Devices: Effect of Naphthyl substitution

Excited-state intramolecular proton transfer (ESIPT) is a tautomerization of π -conjugated intramolecular Brøsted acid and base moieties after photo-excitation. ESIPT materials show uniquely large Stokes shifted emission without self-absorption. This is attributed to their different characteristics in ground and excited state. They exist as enol form (E) in ground state possessing E absorption characteristics but converted into keto form (K) in excited-state, subsequently emit K* fluorescence due to the inversion of acidity and basicity of both acid and base. Based on unique large stokes shift and highly fluorescent properties, many ESIPT dyes have been employed for organic electroluminescent devices.^{1, 2, 3}

Electroluminescence based Organic Light Emitting Diodes (OLED) have attracted considerable interests due to their various advantages for display materials, such as fast response time, high contrast ratio and thin thickness.⁴

Applying the appropriate electric voltage leads the injection of holes and electrons into the emitting layer (EML) from the anode and the cathode, respectively. In the EML, each holes and electrons combine to generate exciton composed of 25% singlet and 75% triplet. Electroluminescence occurs when these two types of excitons degrade with light emission.

Up to now, phosphorescent emitting dye, mostly iridium complex, has been regarded as a solution for high efficiency OLEDs because phosphorescent dyes harness 75% triplet and converted 25% singlet by inter-system crossing, consequently achieving 100% internal quantum efficiency (IQE) while fluorescent dyes utilize only 25% singlet.

On the other hands, Adachi et al. recently demonstrated another approaches toward highly efficient EL from pure-organic materials make use of thermally activated delayed fluorescence (TADF) with a relatively small energy gap between their singlet and triplet (ΔE_{S-T}).⁵ In these systems, spatially separated highest occupied molecular orbital (HOMO) and lowest occupied molecular orbital (LUMO) orbitals yield decrease of ΔE_{S-T} and promote efficient TADF process. In contrast to phosphorescent dyes, these types of molecule could utilize original both 25% singlet and 75% converted singlet from triplet to emit fluorescence. However, development of blue-emitting TADF dyes is still limited.

Here, we investigate thermally activated delayed fluorescence (TADF) of blue-emitting dyes; 2-hydroxyphenyl-tetraphenylimidazole derivatives (HPI) derivatives for applications toward triplet exciton-harvesting devices. First observation of TADF on HPI-Ac was reported previously⁶ but the origin of TADF remains unclear. We first performed more detailed investigation for various derivatives. Structure-property relationship study among HPI derivatives endows us more understanding for development of better OLED dyes. As an example, naphthyl groups are incorporated into 4,5-position of HPI to investigate the effects on thermal stability and TADF efficiency. Based on this study, we propose a new mechanism of ESIPT mediated triplet exciton harvesting for highly efficient EL devices.

3.2 Result and Discussion

3.2.1. Molecular design.

Toward optimized EL dyes of HPI framework with appropriate molecular structure, several substituent effects should be considered. Reported substituent effects on HPI molecules are summarized.

- Introduction of electron donating/withdrawing substituent or extension of conjugation on 2-phenyl rings (see Figure 3.1) largely affects

emission color. Color tuning from blue to red was reported and this is explained by well-known nodal plane model.⁷

- Substituent on 1- phenyl ring rarely combined with optical properties due to their small contribution on HOMO and LUMO. However, they change stacking behavior of HPI molecule. Alkyl substituent endows HPI molecule high crystallinity,⁸ while carbazole and oxadiazole groups provide amorphous stacking structure.^{2a}

Up to now, substituent effect on 4,5-phenyl rings have rarely studied. In order to study the effects of 4,5-aromatic substitution. Starting from basic structure HPI, 4,5-naphthyl modified HPIN was designed to investigate the aromatic substitution effects on HPI fluorophore. MeOPI and MeOPIN molecules are designed as non-proton transfer species. (See Scheme 3.1) Incorporation of carbazole group into HPI, HPI-Cbz was reported as excellent EL fluorophore with efficient charge transfer properties and amorphous stacking structures like other carbazole materials. Similarly, HPIN-Cbz was synthesized which is consisted of HPIN with carbazole moiety.

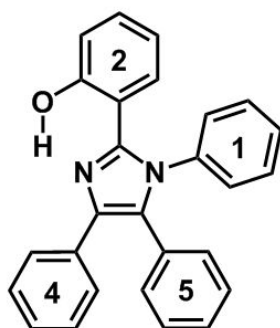
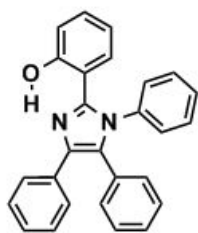
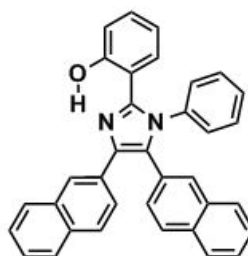


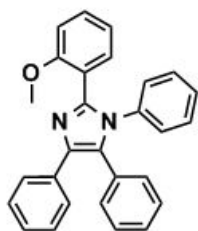
Figure 3.1 Molecular structure and the numbering of phenyl rings of basic HPI molecule.



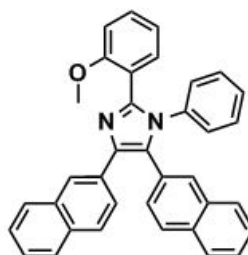
HPI



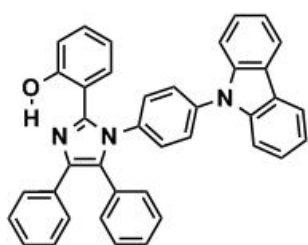
HPIN



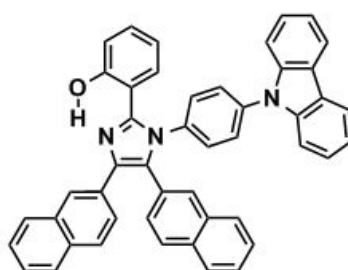
MeOPI



MeOPIN



HPI-Cbz



HPIN-Cbz

Scheme 3.1 Molecular structure of HPI derivatives designed and synthesized.

3.2.2. Optical properties of HPI series molecules.

Figure 3.2 shows the absorption and emission spectra of 10^{-5} M in toluene solution of HPI derivatives in toluene. Upon excitation of E tautomer ($\lambda_{\text{max}} = 320$ nm), four derivatives; HPI, HPI-Cbz, HPIN, HPIN-Cbz undergo ESIPT and emit similar greenish blue fluorescence emission from newly formed K species around 480 nm. Since HPI and HPI, HPI-Cbz and HPIN-Cbz shows exactly same fluorescence maximum of 476 and 483 nm (Table 3.1), respectively. It could be concluded that the extension of conjugation on 4,5-phenyl rings do not affect the fluorescence property. Non-carbazole compounds (HPI, HPIN) show 476 nm maximum while carbazole substituted ones (HPI-Cbz, HPIN-Cbz) emit 483 nm which is 7 nm shifted from the original emission (Figure 3.2). As expected, carbazole moiety rarely affects the fluorescent properties as shown in figure 3.2. Thus, both 1-carbazole and 4,5-naphthyl rarely affects the fluorescence property of HPI derivatives, four compounds possess almost similar singlet energy level.

The small band around 400 nm observed in HPIN, HPIN-Cbz is attributed to E emission of naphthalene substituted compounds which coincides with the emission of MeOPIN molecule and difference between HPI and HPIN (Figure 3.3). To summary, fluorescence property of basic HPI is almost preserved

	Abs. λ_{\max} , 0-0 (eV)	E_g (eV)	Flu. λ_{\max} (eV)	Stokes shift (cm^{-1})
HPI	320 (3.88)	3.50	476 (2.61)	10242
HPI-Cbz	320 (3.88)	3.50	483 (2.57)	10242
HPIN	339 (3.66)	3.31	476 (2.61)	8796
HPIN-Cbz	337 (3.68)	3.31	483 (2.57)	8970

Table 3.1 Optical property of HPI derivatives in toluene solution

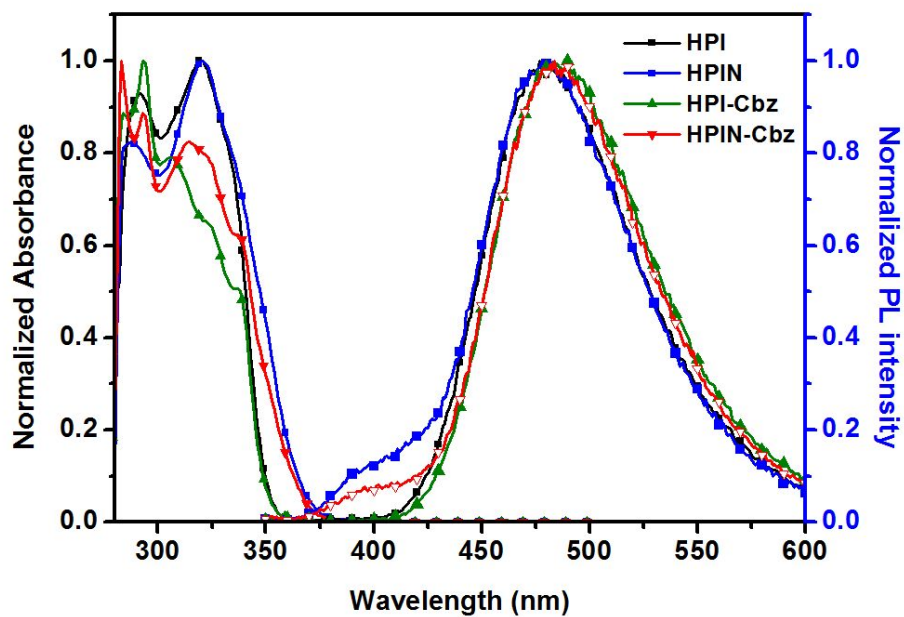


Figure 3.2 Normalized absorbance and PL of HPI, HPI-Cbz, HPIN, HPIN-Cbz compounds.

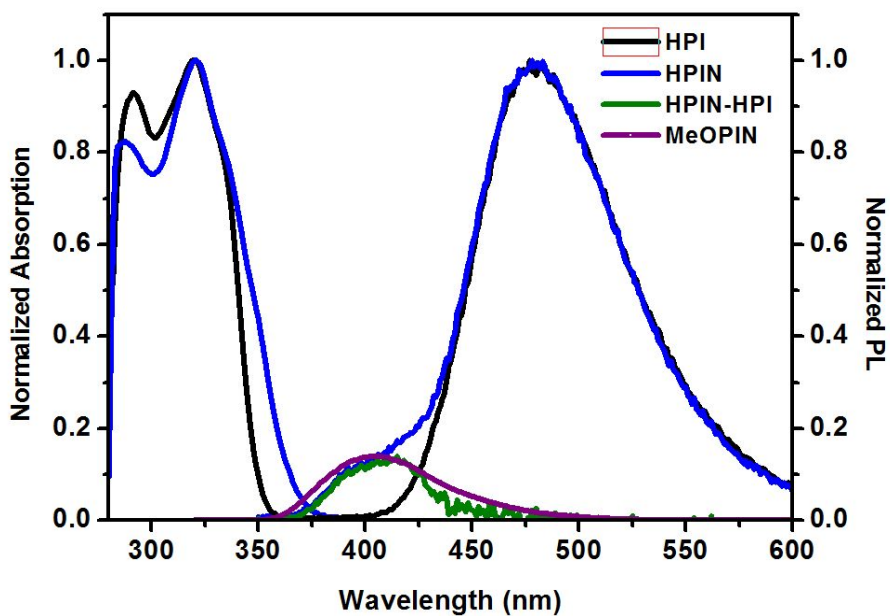


Figure 3.3 Normalized absorbance and normalized HPI, HPIN, their difference and comparison with MeOPIN.

through the substitution of both carbazole and naphthyl.

All compounds exhibit intense emission in solid-state. Photoluminescence quantum yields (PLQY) of solid state increased nearly twice than those in solution. As previously reported from single crystal X-ray analysis of HPI, the steric crowding of the four phenyl groups attached to the central imidazole unit is a key feature to avoid excessive tight stacking.⁶ As a consequence, suppression of intramolecular/intermolecular vibronic coupling leads the enhanced emission of HPI derivatives. In HPI, the substituted phenyl rings at the 1- and 5- position of imidazole ring assumed large dihedral angles near 90° while the 2- and 4-substituted phenyl rings formed a coplanar structure with the imidazole ring by intramolecular hydrogen bonds necessary for the ESIPt process. Based on the results of quantum chemical calculation (Gaussian 09 program with B3LYP/6-31g(d,p) basis set), the optimized geometry of all compounds were found to be planar conformation of imidazole and 2-phenyl rings position (Figure 3.4). 5-aromatic rings were slightly twisted (around 30°) while 2- and 4-substituent were severely distorted (around 60° and 80°), preventing excessive tight stacking. These bulky side groups lead the molecules strongly fluorescent in solid state.

The photophysical properties of four naphthyl and carbazole tuned HPI derivatives are summarized in table 3.2. Compared to isolated solution state,

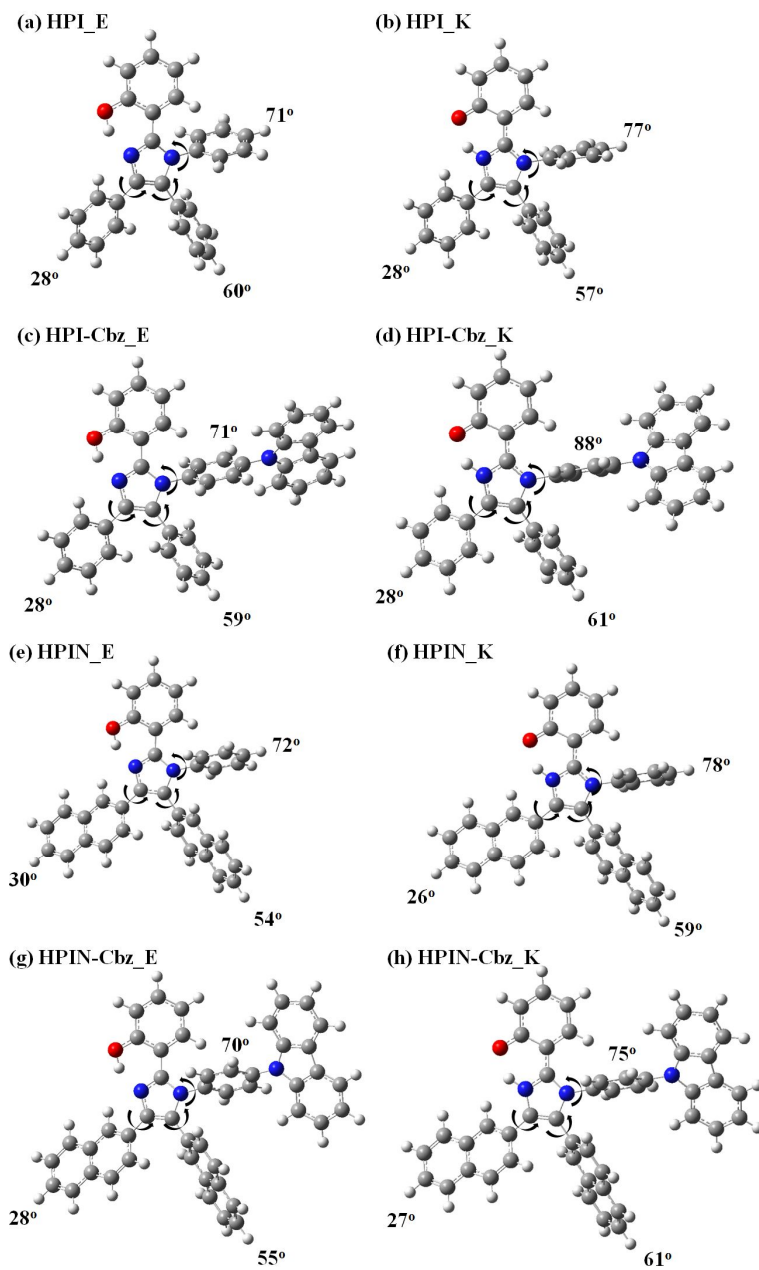


Figure 3.4 Optimized geometry of each tautomer of four compounds. E and K corresponds enol and keto, respectively.

	Φ_{sol}	Φ_{film}	τ_{sol} (ns)	τ_{film} (ns)	$k_{\text{r, sol}}$ ($10^7/\text{s}$)	$k_{\text{r, film}}$ ($10^7/\text{s}$)	$k_{\text{nr, sol}}$ ($10^7/\text{s}$)	$k_{\text{nr, film}}$ ($10^7/\text{s}$)
HPI	0.15	0.35	1.70	3.57	9.0	9.8	50	18
HPI-Cbz	0.20	0.44	1.66	3.72	12	12	48	15
HPIN	0.07	0.16	1.18	2.38	6.3	6.7	78	35
HPIN-Cbz	0.08	0.40	1.08	2.96	7.4	14	85	20

Table 3.2 Photophysical properties of four naphthyl and carbazole tuned HPI derivatives in solution (10^{-5} M in toluene) state and film (100 nm vacuum deposited on quartz substrate) state

film (solid) state of four compounds shows 2~3 times enhanced photoluminescence quantum yield. It was elucidated that those compounds undergo significant changes on non-radiative constant when they form aggregated film state. Solidification leads non-radiative decay constants of all compounds decrease while radiative constants slightly increase.

The origin of such behavior is mainly attributed to modification of free rotation of four phenyl rings which plays crucial roles in non-radiative decay. Generally in isolated state, HPI compounds go through free rotation of four aromatic rings. But in solid state, the molecular conformation of molecule is rigidified so that the free rotation could be limited. Due to this conformation adjustment, non-radiative constant is significantly limited while radiative constant rarely changes.

3.2.3. Thermal properties of HPI-Cbz and HPIN-Cbz

The weak point of previously reported HPI-Cbz molecule was bad device stability, which mainly seems to originated from low glass transition temperature (T_g) of 101 °C and melting temperature (T_m) of 197 °C.^{2a} Especially for non-doping device or host, it is important to enhance the glass transition temperature (T_g).⁹ The thermal properties of HPI molecules were evaluated by differential scanning calorimeter (DSC) at a rate of 10 K min⁻¹.

Owing to enhanced molecular weight, HPIN-Cbz exhibit sharp melting peak (T_m) of 267 °C and glass transition temperature (T_g) of 121 °C, which are much higher than those of HPI-Cbz (Figure 2.5). Also, high degradation temperature (T_d) 441 °C was obtained (Figure 2.6). According to these data, HPIN-Cbz possesses much durable thermal stability than HPI-Cbz materials, appropriate for the real world applications toward blue OLED dyes.

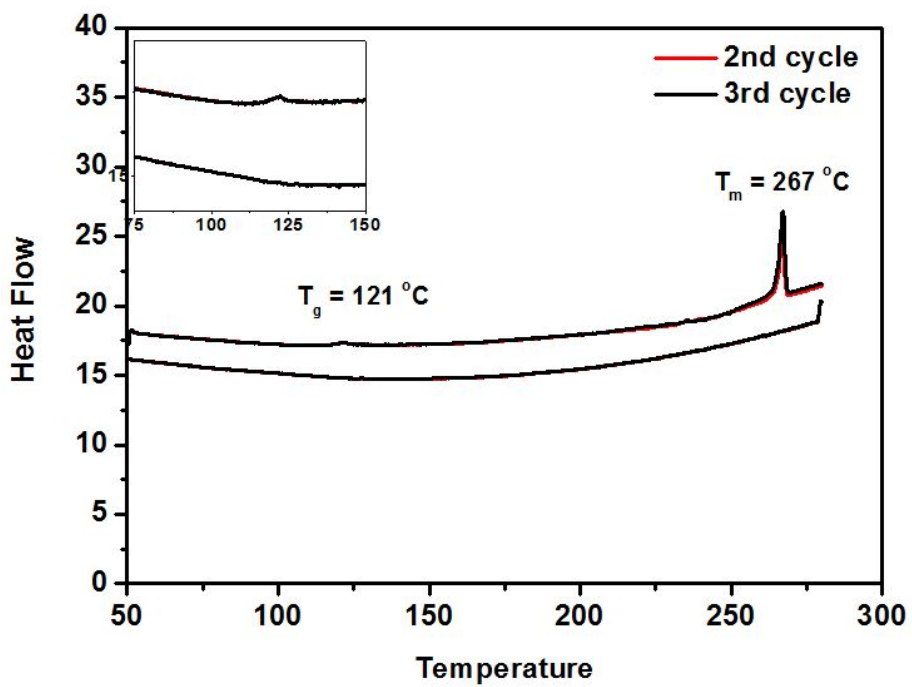


Figure 3.5 Differential scanning calorimetric curve of HPIN-Cbz with scan rate of $10\text{ }^\circ\text{C}/\text{min}$. Inset: magnified graph around glass transition temperature (T_g).

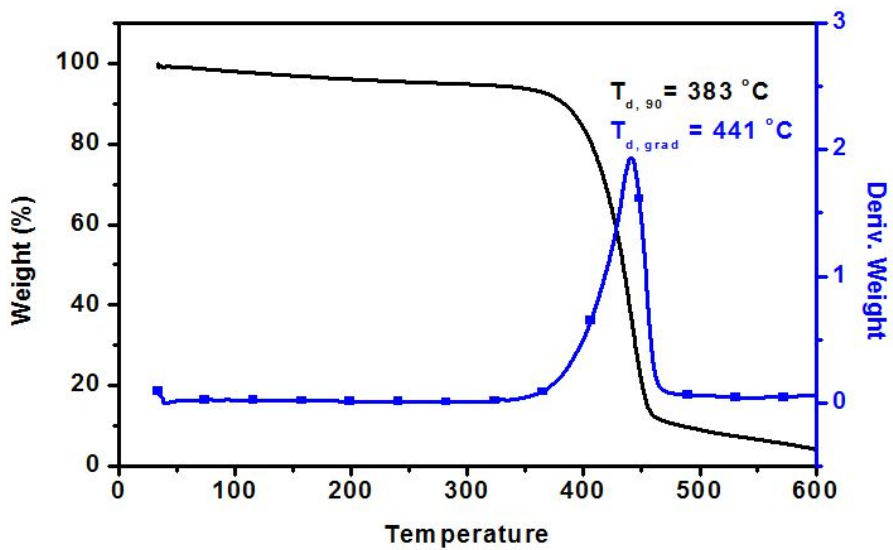


Figure 3.6 Thermo gravimetric analyzer (TGA) curve of HPIN-Cbz with scan rate of 10 °C/min.

3.2.4. Thermally Activated delayed fluorescence (TADF) from HPI derivatives; origin of TADF and temperature dependent behavior.

Figure 3.7 show that the time-resolved emission spectrum of four HPI derivatives collected 100 μ s after photo-excitation at room temperature. Obviously, all delayed spectrum of four compounds exactly coincides with the prompt fluorescence spectrum measured at the moment of photoexcitation. Taking the short decay lifetimes of prompt K fluorescence (several nanoseconds, see Table 3.2) into accounts, it is clear that these emissions are originated from delayed fluorescence. Because phenyl-imidazole core is responsible for the photoluminescence behavior, all HPI derivatives shows the delayed fluorescence.

TADF is observed when T_1 state may thermally popped through the reverse intersystem crossing to reach S_1 state, subsequent fluorescent emission from re-formed S_1 state. In these systems, TADF seems to occur in K form state because the shape of TADF is consistent with K^* fluorescence. (Scheme 3.2) TADF is favored in molecules which own small singlet-to-triplet energy gaps (ΔE_{S-T}). The energy gap between excited singlet (S_1) and excited triplet state (T_1) is given by $\Delta E_{S-T} = 2J_{LU}$.^{10, 5b} Thus, ΔE_{S-T} is proportional to the exchange integral (J_{LU}) between the wave-functions of HOMO and LUMO levels. Quantum chemical calculation (density functional theory with the hybrid

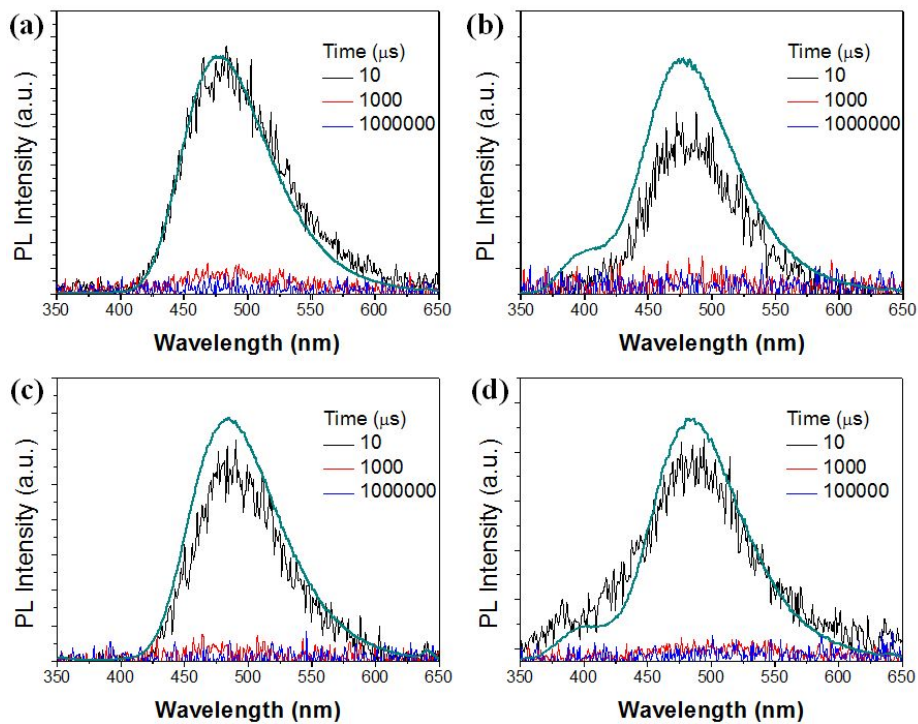
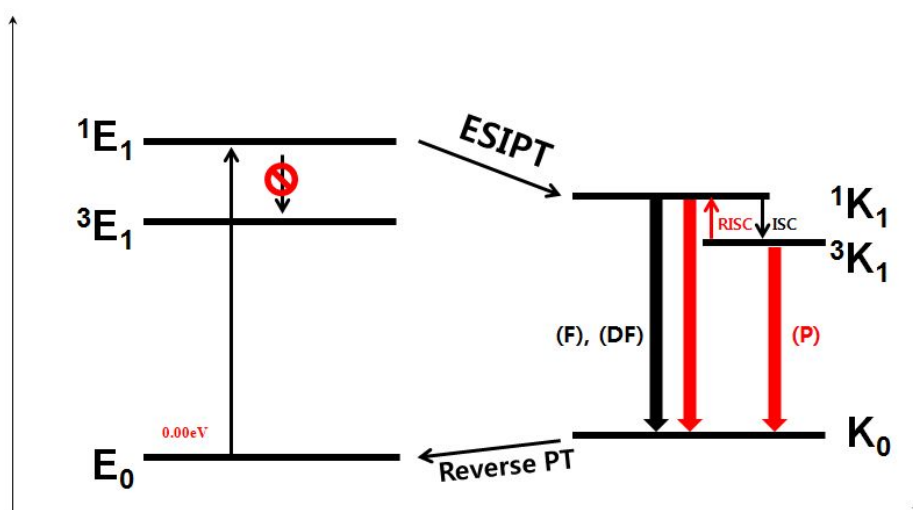


Figure 3.7 time-resolved emission spectrum of (a) HPI (b) HPIN (c) HPI-Cbz (d) HPIN-Cbz collected at prompt (green), after 10 μs (black), 1 ms (red) 1 s (blue) after photo-excitation.



Scheme 3.2 four-level photocycle and delayed fluorescence of HPI series molecule.

method of B3LYP with 6-31g(d,p) basis set) was employed to evaluate these HOMO and LUMO locations of HPI derivatives. The HOMO is localized at 2-phenyl and imidazole ring and the LUMO is localized at 4,5-aromatic rings (Figure 3.8). Due to the tilted conformation of 4,5-aromatic rings induced by steric crowding, the overlaps between HOMO and LUMO orbitals of all HPI derivatives were quite small.

3.2.5. Naphthyl effect on TADF behavior

Figure 3.9-3.12 (a),(b) shows the temperature dependent absorbance change of photoluminescence and time-resolved emission spectrum of tuned HPI derivatives in methyl tetrahydrofuran solution in 2-methyl tetrahydrofuran solution. The temperature dependent delayed fluorescence and phosphorescence were also shown (c), (d). At the low temperature of 77K, all molecules exhibit vibration peaks (Figure 3.9a - 3.12a). A peak around 450 nm is clearly a K* fluorescence emission (Figure 3.9b – 3.12b) while delayed component at 77K is obviously K* phosphorescence emission (Figure 3.9c – 3.12c). Figure 3.9c, d – 3.12c, d show the time-resolved spectra of all compounds at the temperature of 77K (c) and 117K (d). At temperature of 77K, the photoluminescence collected 100 μ s after photoexcitation is assigned to only phosphorescence from triplet K* species. With increasing temperature,

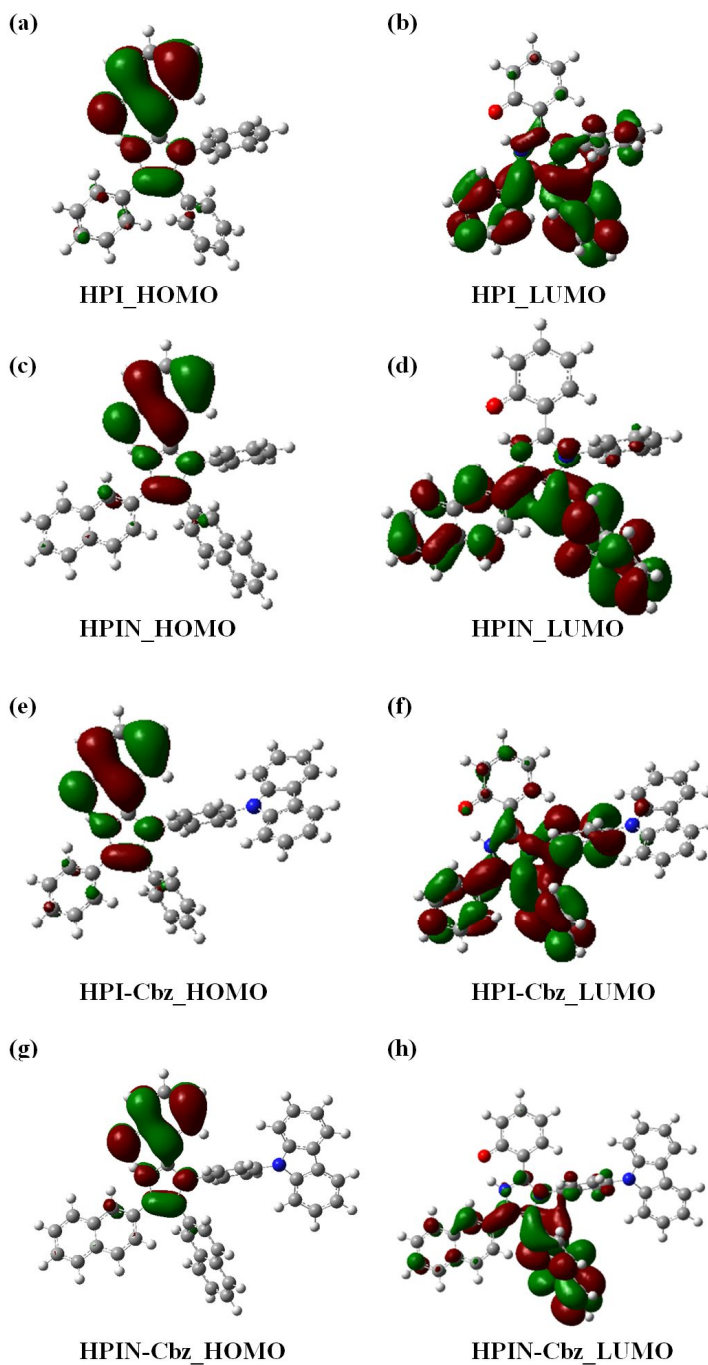


Figure 3.8 Energy level location with optimized geometry of figure 3.4.

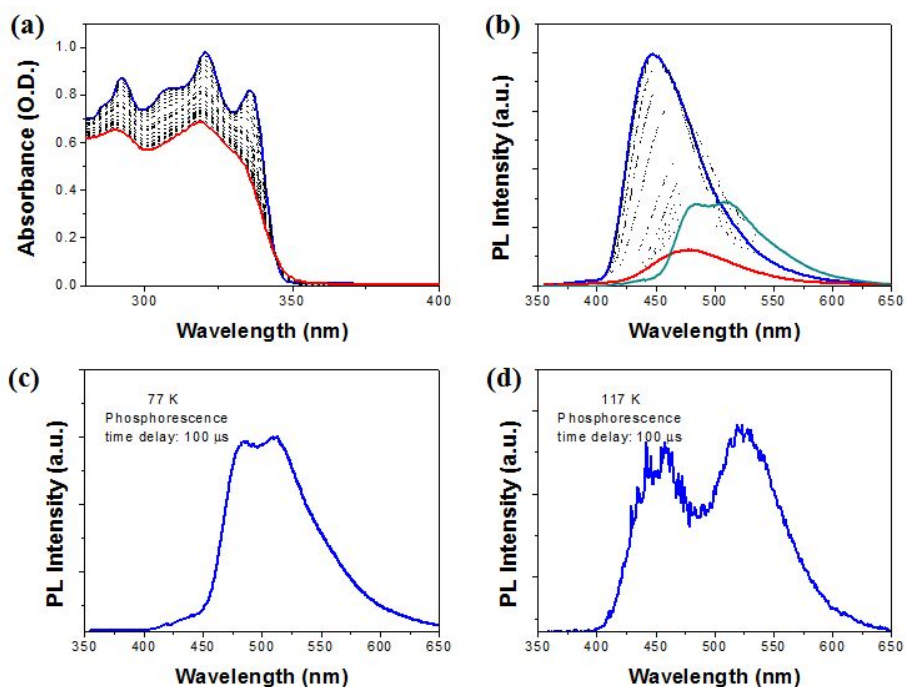


Figure 3.9 (a) Absorbance change of HPI from 298 K (red) to 77 K (red) (b) Photoluminescence change of HPI from 298 K (red) to 77 K (blue) and phosphorescence (green) (c) time-resolved emission spectrum (phosphorescence) of HPI collected 100 μ s after photo-excitation at 77 K (d) time-resolved emission spectrum of HPI collected 100 μ s after photo-excitation at 117 K. Left peak originate from delayed K^* fluorescence while right one is from K^* phosphorescence.

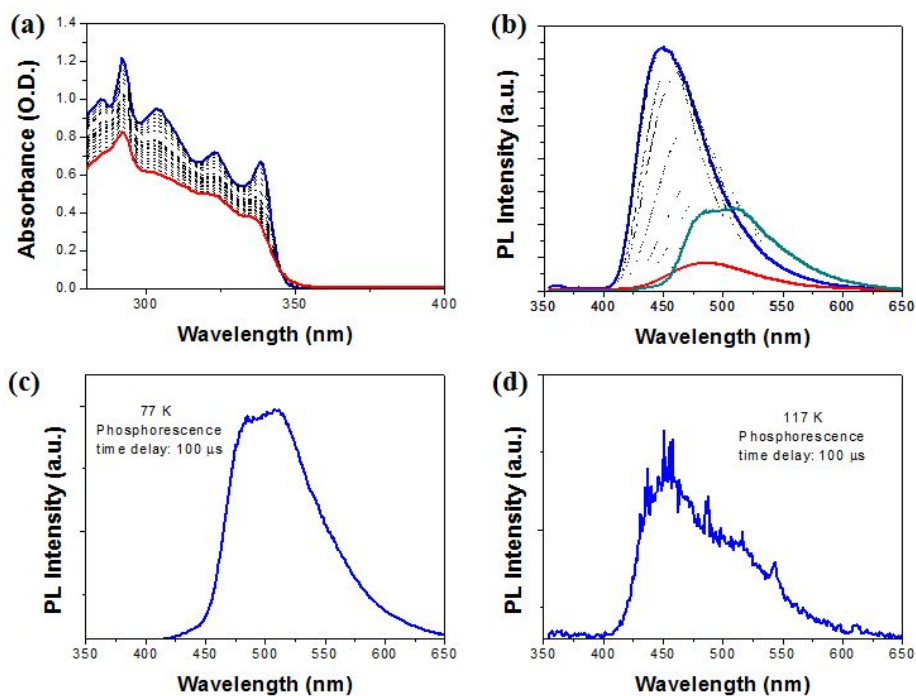


Figure 3.10 (a) Absorbance change of HPI-Cbz from 298 K (red) to 77 K (red) (b) Photoluminescence change of HPI-Cbz from 298 K (red) to 77 K (blue) and phosphorescence (green) (c) time-resolved emission spectrum (phosphorescence) of HPI-Cbz collected 100 μ s after photo-excitation at 77 K (d) time-resolved emission spectrum of HPI-Cbz collected 100 μ s after photo-excitation at 117 K. Left peak originate from delayed fluorescence while right one is from phosphorescence.

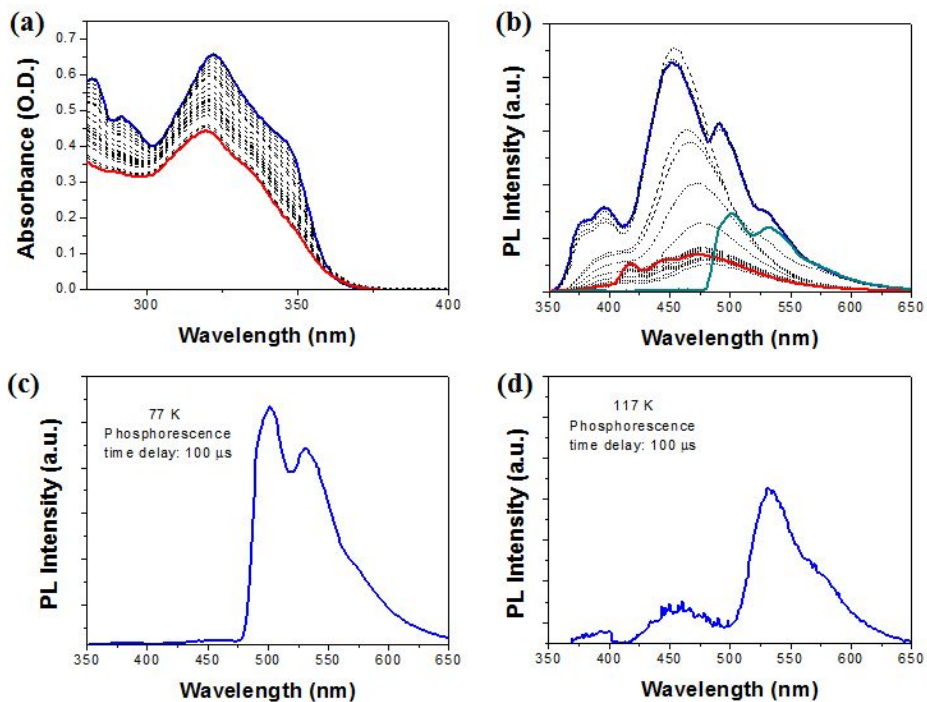


Figure 3.11 (a) Absorbance change of HPIN from 298 K (red) to 77 K (red) (b) Photoluminescence change of HPIN from 298 K (red) to 77 K (blue) and phosphorescence (green) (c) time-resolved emission spectrum (phosphorescence) of HPIN collected 100 μ s after photo-excitation at 77 K (d) time-resolved emission spectrum of HPIN collected 100 μ s after photo-excitation at 117 K. Left peak originate from delayed fluorescence while right one is from phosphorescence.

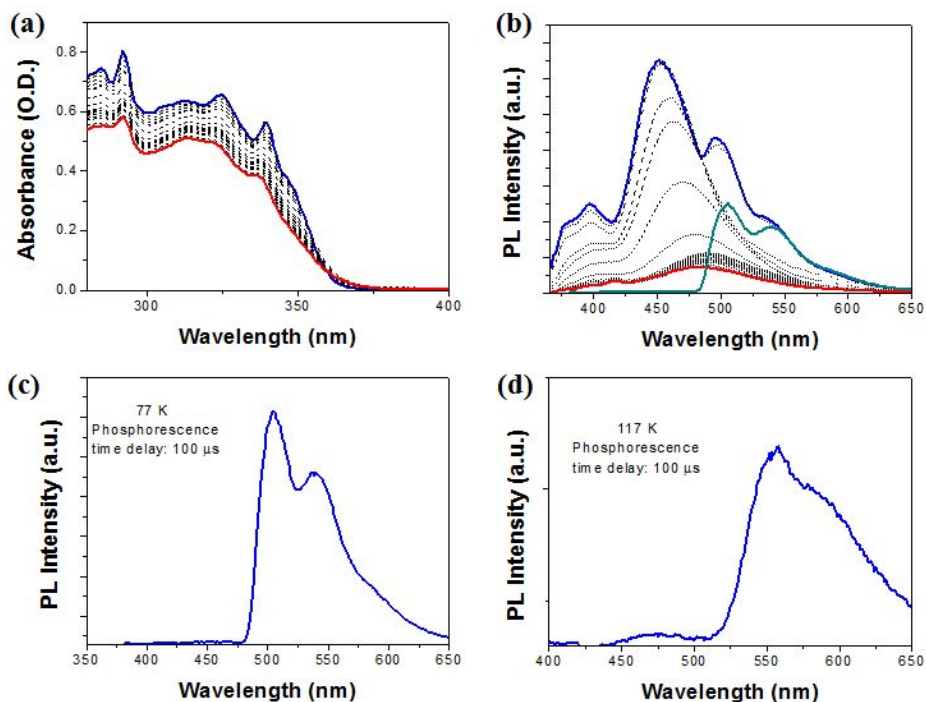


Figure 3.12 (a) Absorbance change of HPIN-Cbz from 298 K (red) to 77 K (red) (b) Photoluminescence change of HPIN-Cbz from 298 K (red) to 77 K (blue) and phosphorescence (green) (c) time-resolved emission spectrum (phosphorescence) of HPIN-Cbz collected 100 μ s after photo-excitation at 77 K (d) time-resolved emission spectrum of HPIN-Cbz collected 100 μ s after photo-excitation at 117 K. Left peak originate from delayed fluorescence while right one is from phosphorescence.

new emission band grows around 450 nm and decrease of phosphorescence is observed. Since TADF is originated from the thermal activation of excited triplet state (T_1), these results well match with the general property of TADF.

Based on fluorescence and phosphorescence maximum, we could estimate the singlet and triplet energy level. The difference between singlet and triplet energy level could be ΔE_{S-T} indicating very small value around 1772 - 2416 cm^{-1} (Table 3.3). Due to these small ΔE_{S-T} , excited triplet state of molecule could easily pop-up to reach singlet excited state through reverse intersystem crossing with a small amount of thermal energy. Especially HPIN, HPIN-Cbz shows higher ΔE_{S-T} , implying the naphthyl substitution leads the increase of ΔE_{S-T} .

3.2.6. Electrochemical properties of HPI derivatives

The HOMO level of HPIN, HPIN-Cbz was evaluated to be 5.4 eV and 5.5 eV, respectively, from the cyclic voltammetry measurement. (Figure 3.13) Also, LUMO was estimated to be 2.1 eV for two compounds from the addition of HOMO level and absorption edge. (Summarized in table 3.4) Previous reported HPI and HPI-Cbz^{2a} possess 5.5 eV and 5.4 eV of HOMO levels which are similar to those of HPIN, HPI-Cbz. Thus, the naphthyl substitution rarely affects the electrochemical properties of HOMO, however,

	Flu λ_{\max} (nm, eV)	Phos λ_{\max} (nm, eV)	ΔE_{S-T} (eV)	ΔE_{S-T} (cm⁻¹)
HPI	447 (2.78)	485 (2.56)	0.22	1772
HPI-Cbz	450 (2.76)	485 (2.56)	0.20	1611
HPIN	452 (2.75)	502 (2.47)	0.28	2256
HPIN-Cbz	451 (2.75)	506 (2.45)	0.30	2416

Table 3.3 Summarized molecular energy level of four HPI derivatives.

	HOMO (eV)	LUMO (eV)
HPI	5.5	1.9
HPI-Cbz	5.4	1.9
HPIN	5.4	2.1
HPIN-Cbz	5.5	2.1

Table 3.4 Estimated molecular orbital energy level of HPI derivatives.

HOMO is from cyclic voltammetry and LUMO comes from the summation of HOMO and optical band gap.

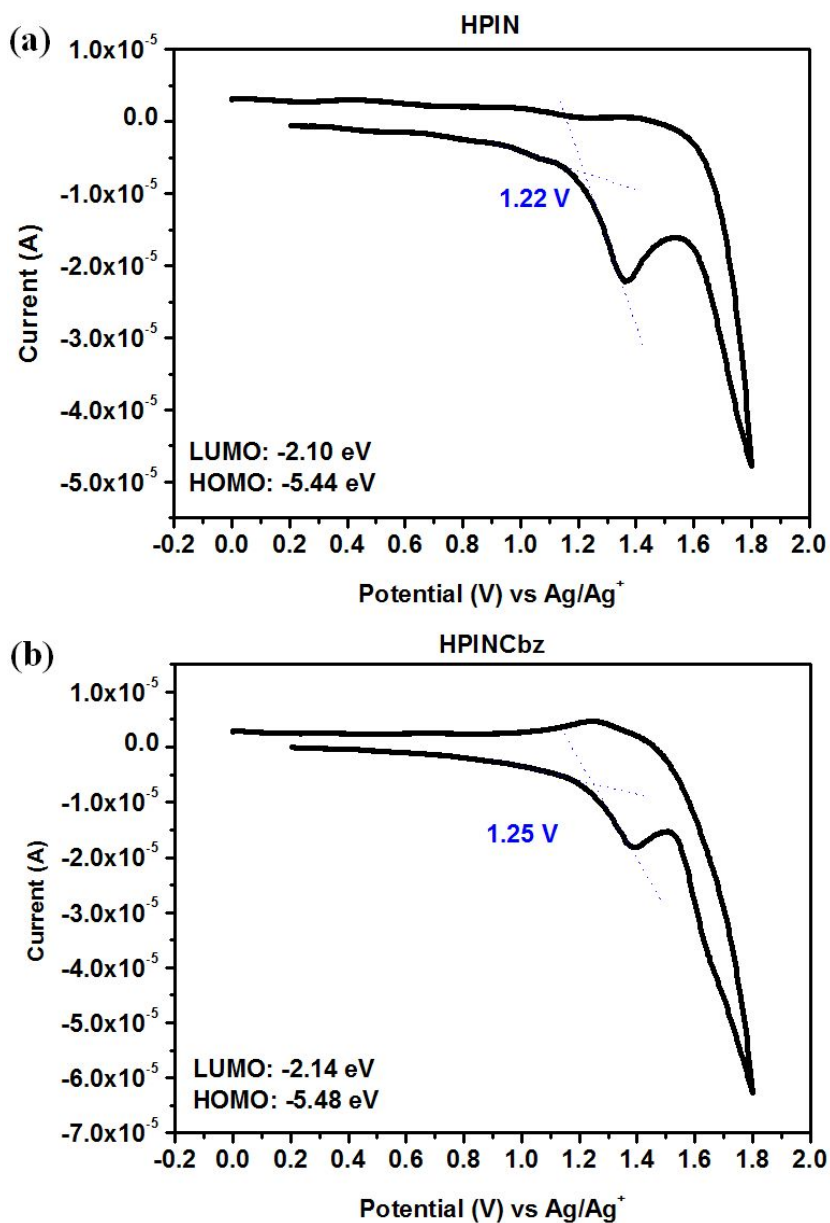
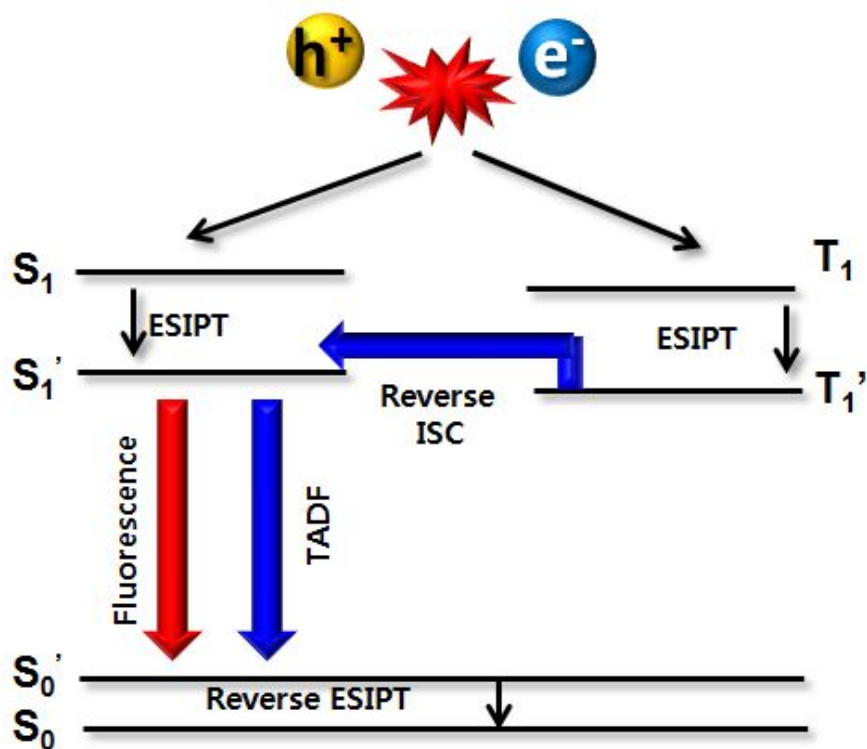


Figure 3.13 Cyclic voltammograms (10^{-3} M solution in dichloromethane, electrolyte: tetrabutylammonium tetraborate, scan rate: 50mV/sec reference electrode: Ag/Ag⁺): (a) HPIN, (b) HPIN-Cbz.

lower LUMO levels. Lowering LUMO level of HPI compounds is beneficial for electron injection because very high LUMO level of previous HPI and HPI-Cbz (1.9 eV) was one of the main barrier of efficient electroluminescence devices.

3.2.7. Proposed spin-harvesting EL mechanism

Spin-harvesting nature of EL device composed of ESIPT fluorescent dye has not reported yet. At previous reports, the external quantum efficiency (EQE) of EL device composed of HPI-Cbz shows 2.94% EQE which is higher than theoretical value (2.2%). However, the origin of these enhanced EQE remains unclear. Here, we propose a mechanism that this HPI-Cbz takes advantage of singlet excitons as well as triplet excitons by spin-up conversion by TADF. The schematic view of spin-up conversion is illustrated on scheme 3.3. HPI series molecules not only harness singlet excitons through the ESIPT process, but also utilize triplet excitons by TADF process. Since, triplet level of E is higher than that of K, triplet generated by electrical excitation undergo ESIPT to reach triplet of K, subsequent TADF process alter the triplet excitons to singlet excitons leading spin-harvesting devices.



Scheme 3.3 Proposed spin-harvesting process of HPI molecules.

3.3 Conclusion

The naphthyl substitution effects of HPI series molecule on thermal properties and photophysical properties were studied. There is a trade-off; substituted naphthyl enhance the thermal stability by increasing glass transition temperature of original molecules and lower LUMO level for efficient electron injection, however, enlarge ΔE_{S-T} to diminish spin-harvesting property.

Also, it is elucidated that the ESIPT process in these derivatives narrows the singlet-to-triplet energy gap (ΔE_{S-T}) since the spatially separated HOMO and LUMO, so that small ΔE_{S-T} of keto species promotes efficient TADF process. Based on these observations, we propose a mechanism that such HPI derivatives could be a spin-harvesting device for highly efficient EL devices.

3.4 Experimental

3.4.1 General Information

Commercially available salicylaldehyde, ammonium acetate, glacial acetic acid, 2-methoxybenzaldehyde, 2-naphthaldehyde, sodium cyanide and all kinds of solvent were purchased from Sigma Aldrich Chemical Co. and used without further purification. ^1H NMR were measured with a Bruker-300 spectrometer and ^{13}C NMR were measured with a Bruker-500 using chloroform-d as a solvent with tetramethylsilane as the internal. High resolution mass spectroscopy (HRMS) was investigated with a JEOL JMS-700. Elemental analysis was measured with an EA1112 (CE Instrument, Italy). Steady state absorbance, fluorescence excitation and emission spectra were recorded in an Uvikon 933 (Kontron) and a Fluoromax 3 (Jobin Yvon Horiba) with concentration of the solute 10 μM . Each fluorescence spectrum was corrected by detector sensitivity and distracted by baseline. Gaussian 09 and GaussView 5.0 have been employed for quantum chemical drawing and calculation. The geometry of the ground-state structures were optimized by the density functional theory using the hybrid B3LYP functional with the split-valence polarized 6-31g (d,p) basis set for all species. To obtain estimates of the vertical electronic excitation energies that include some

account of electron correlation, time-dependent density functional theory (TD-DFT) calculations with the B3LYP functional and 6-31g(d,p) basis set were employed. B3LYP corresponds to the combination of Becke's three parameter exchange functional (B3) with a Lee-Yang-Parr fit for the correlation functional (LYP).

3.4.2 Synthesis

Synthesis of 1,2-di(naphthalen-2-yl)ethane-1,2-dione is based on previous report.¹¹

2-(1-(4-(9H-carbazol-9-yl)phenyl)-4,5-di(naphthalen-2-yl)-1H-imidazol-2-yl)phE (HPIN-Cbz) : 1.57 g of salicylaldehyde (12.9 mmol) and 3.33g of 4-(9H-carbazol-9-yl)aniline (12.9 mmol) were dissolved in 100 mL of glacial acetic acid and heated at 60 °C. After 3 h, 4.00 g of 1,2-di(naphthalen-2-yl)ethane-1,2-dione (12.9 mmol) and 6.96 g of ammonium acetate (90.3 mmol) were added subsequently. The mixture was heated at 110 °C for 12 h. After termination of the reaction, the dark black solution was poured into 500 mL water. After neutralization, the black suspension was filtered and residue was recrystallized in 400 mL hot methanol. 3.43 g of white HPIN-Cbz powder was obtained. (Yield = 41%) ¹H NMR (300

MHz, CDCl₃, 298 K, ppm) δ = 13.37 (s, 1H), 8.22 (s, 1H), 8.13 (d, 2H, 7.5 Hz), 8.87 (d, 1H, 8.0 Hz), 7.81 (d, 1H, 8.4 Hz), 7.79-7.64 (m, 6H), 7.60-7.27 (m, 14H), 7.25-7.15 (m, 3H), 6.86 (d, 1H, 7.92 Hz), 6.53 (t, 1H, 7.89 Hz).
¹³C NMR (125 MHz, CDCl₃, 298 K, ppm) δ = 158.57, 145.39, 140.41, 138.46, 136.05, 135.99, 133.49, 133.11, 132.94, 132.63, 131.12, 130.71, 130.45, 130.35, 128.45, 128.39, 128.26, 128.18, 127.82, 127.58, 127.07, 126.98, 126.59, 126.27, 126.16, 126.11, 125.89, 125.28, 123.62, 120.46, 118.13, 118.00, 112.91, 109.33. HRMS (FAB, positive): calc. for C₄₇H₃₁N₃O [M]⁺ 653.2467; found 654.2537. Elemental Analysis: calc. for C 86.35, H 4.78, N 6.43; found C 86.08, H 4.82, N 6.31

2-(2-methoxyphenyl)-4,5-di(naphthalen-2-yl)-1-phenyl-1H-imidazole

(MeOPIN) : 0.40 g of 2-methoxybenzaldehyde (1.61 mmol) and 0.27 g of aniline were dissolved in 10 mL of glacial acetic acid and heated at 60 °C. After 3 h, 0.50 g of 1,2-di(naphthalen-2-yl)ethane-1,2-dione (1.61 mmol) and 1.57 g of ammonium acetate (11.3 mmol) were added subsequently. The mixture was heated at 110 °C for 12 h. After termination of the reaction, the dark black solution was poured into 300 mL water. After neutralization, the black suspension was filtered. Silica column chromatography was carried out twice, with the eluent of ethyl acetate: n-hexane = 1:3 and chloroform:e

ethyl acetate: n-hexane = 1:1:3. White powder of MeOPIN 100 mg was obtained (Yield = 13%)

3.5 References

1. J. E. Kwon and S. Y. Park, *Adv. Mater.* **2011**, 23, 3615.
2. (a) S. Park, J. Seo, S. H. Kim and S. Y. Park, *Adv. Funct. Mat.* **2008**, 18, 726-731; (b) D. Ma , F. Liang , L. Wang , S. T. Lee , L. S. Hung , *Chem. Phys. Lett.* **2002** , 358 , 24.
3. (a) S. Park, E. K. Ji, H. K. Se, J. Seo, K. Chung, S. Y. Park, D. J. Jang, B. M. Medina, J. Gierschner and S. Y. Park, *J. Am. Chem. Soc.* **2009**, 131, 14043; (b) K.-C. Tang, M.-J. Chang, T.-Y. Lin, H.-A. Pan, T.-C. Fang, K.-Y. Chen, W.-Y. Hung, Y.-H. Hsu and P.-T. Chou, *J. Am. Chem. Soc.* **2011**, 133, 17738.
4. C. W. Tang and S. A. Vanslyke, *Appl. Phys. Lett.* **1987**, 51, 913.
5. (a) A. Endo, M. Ogasawara, A. Takahashi, D. Yokoyama, Y. Kato and C. Adachi, *Adv. Mater.* **2009**, 21, 4802; (b) K. S. Ayataka Endo, Kazuaki Yoshimura, Takahiro Kai, Atsushi Kawada, Hiroshi Miyazaki, and Chihaya Adachi, *App. Phys. Lett.* **2011**, 98, 083302; (c) K. Goushi, K. Yoshida, K. Sato and C. Adachi, *Nat. Photon.* **2012**, 6, 253.

6. S. Park, O. H. Kwon, Y. S. Lee, D. J. Jang and S. Y. Park, *J. Phys. Chem. A*, **2007**, 111, 9649.
7. S. Park, J. E. Kwon and S. Park, *Phys. Chem. Chem. Phys.* **2012**.
(Accepted) DOI: 10.1039/C2CP23894B
8. S. Park, O.-H. Kwon, S. Kim, S. Park, M.-G. Choi, M. Cha, S. Y. Park and D.-J. Jang, *J. Am. Chem. Soc.* **2005**, 127, 10070.
9. J. Li, D. Liu, Y. Li, C.-S. Lee, H.-L. Kwong and S. Lee, *Chem. Mater.* **2005**, 17, 1208.
10. Turro, N. J. *Modern Molecular Photochemistry*, University Science Books, Sausalito, California, **2009**.
11. L. E. Harrington, J. F. Britten, D. W. Hughes, A. D. Bain, J.-Y. hépot and M. J. McGlinchey, *J. Organomet. Chem.* **2002**, 656, 243.

Abstract in Korean

초 록

여기상태 분자내 양성자 이동 물질의 합성, 광물리 과정 분석 및 응용

이 종 하

공과대학 재료공학부

서울대학교 대학원

여기상태 분자내 양성자 이동 (ESIPT) 현상을 보이는 분자들은 자기 흡수가 없고 강한 형광을 발현하는 성질, 그리고 주위 환경에 민감하게 형광색이 변하는 성질로 인하여 유기발광소자, 형광센서, 유기레이저 등으로의 연구가 활발하다. 본 연구에서는 새로운 형태의 여기상태 분자내 양성자 이동 현상을 보이는 물질들이 고체 상태에서 강한 형광이 보이도록 설계하고, 그 안에서 일어나는 광물리과정을 연구하여 이의 응용 가능성에 관하여 진행한 연구에 대하여 보고한다. 합성된 물질들은 모두 용액 상태에서보다 고체

상태에서 형광이 높아지는 “집합체 유도에 의한 형광 증진 현상 (AIEE)”을 보였다. 이는 집합체 유도에 의한 분자 평면화 및 J-형태 회합체 형성과 분자 내 회전운동의 금지를 통한 형광성 이완의 증진에 의한 것이다.

이를 바탕으로 뛰어난 자기조립 능력을 지니는 살리실리덴-아닐린 기반의 분자를 합성하였으며, 1차원 구조를 이룸으로써 강한 형광을 보이는 것을 확인하였다. 또한 생물학적으로 중요한 불소 이온의 첨가 시에 젤-졸 상변이와 형광색 변화를 유발하는 형광젤 시스템이 구현되었으며 이는 향후 음이온 검출 키트로의 활용이 기대된다.

고체 상태에서 강한 형광을 보이는 이미다졸 분자들은 이전까지 활발히 연구되어 유기발광소자로서 활용되었으며, 이에서 발견되는 지연형광 현상이 보고되었다. 본 연구에서는 더 나은 유기발광소자로서의 활용 가능성을 위하여 나프틸그룹이 치환된 이미다졸 분자들의 열적, 전기화학적, 광학적 성질에 관한 실험을 진행하였다. 나프틸 그룹이 치환된 물질들은 고체상태에서 보다 강한 형광을 가지는 것이 측정되었다. 또한 기존의 물질과 비슷한 형광파장을 가지면서도 높은 유리 전이 온도 (glass transition temperature)를 가져 열적으로 더 안정하고, 좀 더 낮은 비점유 분자궤도함수 (LUMO) 레벨로 인하여 전자의 주입이 좀 더 쉬운 장점을 가지고 있어 좀 더 나은 유기발광소자로서의 가능성을

가지는 것을 확인하였다. 마지막으로, 이미다졸 분자들에서 공통적으로 발견되는 지연 형광을 응용한 스핀 하비스팅 (spin-harvesting) 소자로써의 가능성을 제시한다.

주요어: 여기상태 분자내 양성자 이동, 집합체 유도에 의한 형광 증진 현상, 지연 형광, 스마트젤, 전기 발광, 스핀-하비스팅.

학 번: 2010-22766

List of Presentations

1. Jong Ha Lee, Ji Eon Kwon, Soo Young Park, "A Novel Salicylideneaniline-based Organogelator with Gelation Induced Emission Enhancement and Excited-State Intramolecular Proton Transfer", The 105th Spring Meeting of the Korean Chemical Society, April 29-30, 2010, Songdo, Korea.